Science and Technology of Advanced Materials

ISSN: 1468-6996 (Print) 1878-5514 (Online) Journal homepage: www.tandfonline.com/journals/tsta20

Strategies to improve the thermoelectric performance of iron silicide-based materials

Sopheap Sam, Sreypich Say, Kosuke Yamazaki & Hiroshi Nakatsugawa

To cite this article: Sopheap Sam, Sreypich Say, Kosuke Yamazaki & Hiroshi Nakatsugawa (10 Nov 2025): Strategies to improve the thermoelectric performance of iron silicide-based materials, Science and Technology of Advanced Materials, DOI: 10.1080/14686996.2025.2585555

To link to this article: https://doi.org/10.1080/14686996.2025.2585555

Publisher: Taylor & Francis & The Author(s). Published by National Institute for Materials Science in partnership with Taylor & Francis Group.
Journal:*Science and Technologyof Advanced Materials*
DOI: 10.1080/14686996.2025.2585555

Strategies to improve the thermoelectric performance of iron silicide-based materials

Sopheap Sam[1,2,*], Sreypich Say[3], Kosuke Yamazaki[4], and Hiroshi Nakatsugawa[4]

[1] *Department of Industrial and Mechanical Engineering, Faculty of Electrical Engineering, Institute of Technology of Cambodia, Russian Federation Blvd, P.O. Box 86, Phnom Penh 120404, Cambodia*

[2] *Research and Innovation Center, Institute of Technology of Cambodia, Russian Federation Blvd, P.O. Box 86, Phnom Penh 120404, Cambodia*

[3] *University of Puthisastra, 55, 180, Phnom Penh 12211, Cambodia*

[4] *Graduate School of Engineering Science, Yokohama National University, 79-5 Tokiwadai, Hodogaya, Yokohama, Kanagawa 240-8501, Japan*

* Corresponding authors: sam.sopheap@itc.edu.kh (S. Sam)

Abstract

Iron silicide (β-$FeSi_2$) has attracted considerable interest as a sustainable thermoelectric material due to its abundance, non-toxicity, and environmental compatibility. Their conduction flexibility allows a wide range of dopants to tune transport behavior, creating opportunities for improved performance. However, dopant solubility limits and the formation of secondary phases remain key challenges. In this article, we highlight recent advances in strategies to enhance the thermoelectric performance of β-$FeSi_2$-based materials and discuss the interplay between phase evolution, electrical, and thermal transport. We also outline prospects that may unlock further improvements, offering pathways toward higher thermoelectric efficiency in this material system.

Keywords: Iron silicide, Structural properties, Transport properties, Thermoelectric materials.

I. Introduction

Thermoelectric (TE) generators are a solid-state device that could harvest waste heat and directly convert it into electricity without any moving parts or chemical pollution released to the environment [1,2]. The performance of the TE device is primarily related to the materials' performance, as measured by the dimensionless figure of merit (*ZT*). The *ZT* value of a material is defined by: $ZT=S^2\rho^{-1}\kappa^{-1}T$, where *S* is the Seebeck coefficient, ρ is the electrical resistivity, *T* is the temperature, and κ is the total thermal conductivity dominated by electronic and lattice thermal conductivity ($\kappa = \kappa_e + \kappa_l$). In addition, the power factor (*PF*) of a material is expressed by: $PF = S^2\rho^{-1}$ [3]. The improvement of *ZT* value can be achieved by increasing *PF* and reducing κ. Typically, materials with acceptable conversion efficiency, such as Pb, Bi, and Te in PbTe and Bi_2Te_3 [4–10], are either rare or toxic. Therefore, researchers attempted to optimize the transport properties of abundant and less/non-toxic compounds such as oxides [4–7], Heusler [8–13], and silicide [14–23]. Among silicide compounds, iron silicide is a promising TE material due to its oxidation resistance, thermal stability, and ability to operate at high temperatures [23–25]. As shown in **Fig. 1**, iron silicide can be crystallized in three phases, namely tetragonal α-phase (α-Fe_2Si_5, *P4/mmm* space group) [26], cubic ε-phase (ε-FeSi, $P2_13$ space group) [27], and orthorhombic β-phase (β-$FeSi_2$, *Cmce* space group) [28–30]. Based on the Piton and Fay [15], the semiconducting β-phase can be obtained at growth temperatures below 1259 K, and its formation is influenced by the type and concentration of dopants. It should be noted that pristine ε-FeSi is a narrow-gap semiconductor [31]; however, it can exhibit metallic-like

behavior when doped or when present as a secondary phase due to impurity-induced metallization, and α-Fe_2Si_5 also exhibits metallic behavior. Therefore, they are unsuitable for thermoelectric applications due to their negative impact on the Seebeck coefficient ($S = -\Delta V/\Delta T$, where ΔV is the thermoelectric voltage and ΔT is the temperature gradient across the material). In contrast, β-iron silicide (β-$FeSi_2$) is a semiconductor with a bandgap of ~0.7 eV that has gained attention in TE applications.

It should be noted that the performance of pure β-$FeSi_2$ is still limited due to its low carrier density ($n \sim 10^{16}$ cm^{-3}) and narrow bandgap (E_g~0.7 eV) [32,33], leading to high electrical resistivity and bipolar effect, respectively. The bipolar effect has a negative impact on $|S|$. **Fig. 2 (a)** explains the phenomenon of how the bipolar effect at low n contributes to the reduction in $|S|$. The Seebeck effect arises from two types of charge carriers (electrons and holes) with opposite polarities. At elevated temperatures and low carrier density, their opposing contributions can cancel each other out, reducing the overall Seebeck effect, which is an undesirable outcome for thermoelectric applications [34–36]. These issues can be solved by increasing the carrier density of the system. **Fig. 2 (b)** explains the mechanism of reducing the bipolar effect by increasing carrier density for n-type material. When the carrier density of electrons increases, the majority of charge carriers are electrons; hence, the $|S|$ can be improved in high-temperature regions. The same concept is applied to p-type materials when the carrier density of holes is improved. Importantly, the enhancement of carrier density contributes not only to the reduction of the bipolar effect but also to the decrease in electrical resistivity, resulting in an improvement in power factor.

The carrier density of β-$FeSi_2$ can be effectively enhanced by doping impurities into either Fe or Si sites. In addition, the conduction properties of β-$FeSi_2$ can be tuned into both n-type and p-type. The increase in carrier density of electrons of n-type materials can be obtained by doping elements having more valence electrons into the Fe or Si site. On the other hand, the increase in carrier density of holes of p-type can be obtained by doping with elements having fewer valence electrons. For example, the n-type β-$FeSi_2$ can be obtained by substituting Co or Ni into the Fe site, while the p-type ones can be achieved by doping Mn or Cr. The doping strategy could not only contribute to enhancing *PF* but also reduce thermal conductivity. A recent study found that cobalt (Co) dopant introduces the strain to β-$FeSi_2$, leading to lattice softening. The lattice softening reduces phonon speed and consequently reduces lattice thermal conductivity [37]. In addition, Qui *et al*. [38] reported that Ir doping had high solubility ~ 16% in n-type β-$FeSi_2$, resulting in significant improvement in *PF* values. Ir atoms also act as heavy elements to reduce the thermal conductivity of β-$FeSi_2$ down to 2.8 $Wm^{-1}K^{-1}$ at room temperature. As a result, the maximum *ZT* of 0.6 at 1000 K was obtained by Ir doping. Such a *ZT* value is comparable to or even higher than other conventional TE materials, such as Heusler alloys [13,39] and oxide materials [40–42]. The addition of Co and Ni dopants also helps to improve the power factor, but it was found that the amount of impurity phase increases with increasing doping concentration [43]. This tendency was also observed in the samples doped with Mn [44], Al [45], and Cu [46]. In addition, while attempting to reduce the thermal conductivity by doping with heavy elements such as Ge [45] and Ru [47], the formation of the metallic phase also occurs. It is important to note that the presence of a secondary metallic phase has a negative impact on TE performance. When the dopants reach their solubility limit, the

formation of secondary metallic phases (ε and α-phases) in β-$FeSi_2$ is dominant. As a result, this limits the improvement in carrier density and deteriorates the |*S*|. To improve the dopant's solubility, it is necessary to understand how the structure changes with the doping level and its relation to the electrical and thermoelectric properties.

In this article, we review recent progress in doping strategies, structural modifications, and property optimization of β-$FeSi_2$, a non-toxic and low-cost thermoelectric material. We discuss the mechanisms of dopant incorporation, their influence on carrier concentration and mobility, and the resulting impact on thermoelectric performance. We also discuss current challenges, emerging approaches, and future research opportunities toward realizing high-performance β-$FeSi_2$-based thermoelectric materials.

II. Structural transition of β-$FeSi_2$-based materials

The X-ray diffraction (XRD) patterns are commonly used to identify the crystal structure of the fabricated materials [48,49], while the scanning electron microscope (SEM) is used to observe the variation in microstructures. The formation of secondary metallic phases (ε-FeSi and α-Fe_2Si_5) in β-$FeSi_2$ is very sensitive to the dopants. The presence of secondary phases can be observed by both XRD and SEM. First, we discuss the observation of the presence of the metallic phase in β-$FeSi_2$ using the XRD pattern. **Fig. 3** shows the result of Rietveld analysis from XRD data for non-doped $FeSi_2$, 10% Co-doped, and 10% Mn-doped samples prepared by arc melting and heat treatment process [43,44]. In **Fig. 3 (a)**, the non-doped sample was crystallized in semiconducting β-phase, as confirmed with the indexed peaks. There is also a trace of ε-phase (at 2θ = 45.2°) as observed on the right side of the 421 peak. However, the intensity of this ε-

phase is much lower than that of the sample with 10% Co and 10% Mn doping, as illustrated in **Fig. 3 (c-d)**. In addition, it is shown that the α-phase (at 2θ = 37.6°) is also dominant with the addition of dopants Co and Mn. Therefore, the XRD patterns could tell us the presence of secondary phases, and their peak intensities increase with increasing dopants. Regarding the lattice parameters, it was reported that the lattice constants and volume tend to increase with increasing doping levels of Co [33,50], Mn [44], and Ir [38]. This is because when substituting the dopants into the β-$FeSi_2$, the atomic size of Co (r_{Co} = 1.26 Å), Mn (r_{Mn} = 1.39 Å), and Ir (r_{Ir} = 1.37 Å) is larger than that of Fe (r_{Fe} = 1.25 Å). Nishida *et al.* mentioned that the increase in lattice constants indicates that the Co atoms are dissolved in the solid solution of β-$FeSi_2$ [50]. But our research group found that even though the lattice constant keeps increasing up to 10% Co doping [33], the amount of β-phase remarkably drops to ~ 70% at a doping level of ≥ 7% Co [43]. The remarkable decrease in β-phase indicates that dopants reach their solubility limits in β-$FeSi_2$. The degradation of the β-phase at various doping levels of Mn, Co, and Ni [43,44,51] is reported in **Fig. 4 (a)**. As shown in **Fig. 4 (b)**, the lattice constant of β-$Fe_{1-x}Mn_xSi_2$ decreases with increasing x, while that of β-$Fe_{1-x}Co_xSi_2$ and β-$Fe_{1-x}Ni_xSi_2$ increases with increasing x. The trend appears not to be strictly monotonic. The deviation from the linear trend is thought to reflect effects such as solid solution limits within the β phase or precipitation of the ε phase or α phase. Such phase evolution can locally modify the lattice structure, leading to the observed non-monotonic behavior. In particular, the lattice constant of β-$Fe_{1-x}Co_xSi_2$ deviates from the linear relationship at $x > 0.06$, strongly suggesting that the lattice constant is directly correlated with the solubility limit via Vegard's law. The tendency indicates that the amount of β-phase in Mn-doped samples is more stable than that of Co and Ni, as the β-

phase could be maintained at ~95% up to 8% Mn doping. This indicates that Mn is more soluble than Co and Ni in the β-$FeSi_2$ system. In addition, Cheng *et al*. [52] recently reported that by prolonging annealing time up to 15 days at 1023 K, the single β-phase could be achieved up to 8% Co doping based on the observation of XRD pattern and SEM images. However, the quantification of phase occupation was not provided. Therefore, it is necessary for every study to investigate the phase fraction when the dopants are introduced to β-$FeSi_2$-based materials, as the formation of a secondary metallic phase negatively impacts the TE performance.

Next, we review how the microstructures of β-$FeSi_2$ change with the addition of dopant. Our group recently employed SEM-EDS techniques to investigate the effect of Ni doping on the microstructure of β-$FeSi_2$ with varying Ni doping levels from 0.5% to 3.0% [53]. As illustrated in **Fig. 5**, for all samples, in the area of the β-phase, the Fe atomic concentration is approximately 1/3, while that of Si is approximately 2/3. This indicates a Fe: Si ratio of about 1:2, corresponding to β-$FeSi_2$. On the other hand, in the area of ε-phase, the Fe: Si ratio is about 1:1, corresponding to the secondary metallic phase of ε-FeSi. Notably, for 0.5% Ni doping, the microstructure shows a single β-phase, and the distribution of all elements is homogeneous, indicating that Ni is well soluble in β-$FeSi_2$. However, the presence of ε-phase is found in ≥1.0% Ni-doping samples, and the grain size of ε-phase increases with the doping level. In addition, the richness of Fe and Ni elements is accumulated in the ε-phase. A similar tendency was observed in Mn-doped samples [44]. Moreover, even if the nominal doping level is 3%, the actual Ni concentration measured in the β-phase was about 1.0% only. This indicates the solid solution limit of Ni in β-$FeSi_2$ is 1.0%. Due to its low solubility, the carrier density of Ni-doped samples is lower than that of other n-type materials, as listed

in **Table 1**. As a result, the maximum *ZT* of only 0.019 is obtained in 0.5% Ni doping due to the small amount of impurity phase. However, such a low value is still far from practical applications. In addition, it was found that the β-phase linearly decreased with Ni addition [43], resulting in decreasing TE performance. However, optimization of annealing conditions (temperature and time) could help to maintain the β-phase while increasing the solid solution of the dopant. For example, based on a recent study [52], the microstructural observation showed that the grain of the ε-phase almost disappeared for 8% Co-doped β-$FeSi_2$ after a long annealing time of 15 days and a lower temperature of 1023 K. More importantly, the microstructure analysis of Qiu *et al*. [38] showed that there was no presence of any impurity phase at a high Ir doping level of 16% at an annealing time of 48 h and temperature of 1173 K, resulting in a maximum *ZT* of 0.6 at 1000 K. On the other hand, Dąbrowski *et al*. [54] investigated the variation of the microstructure of β-$FeSi_2$ with various dopants, including Co, Mn, Al, and P. They found that the grain ε-phase appeared in Co-and Mn-doped samples, but was absent in Al and P-doped ones. In addition, another study by their group showed that the grain of ε-phase increases when alloying with B_4C particles [55]. Therefore, the formation of the impurity phase in the β-$FeSi_2$ system is sensitive not only to the heat treatment condition, but also to the type and concentration of dopants. The observation of microstructure transition is important to understand homogeneity, solubility, and the presence of secondary phase, which has a remarkable contribution toward optimizing the TE properties of silicide-based materials.

The formation of secondary phases, such as ε- and α-phases, is sensitive to the preparation route, and they can readily form during high-temperature processes like arc

melting. For non-doped samples, these secondary phases can be converted to the β-phase ~97% through appropriate annealing, as confirmed by Rietveld refinement [43]. Dopants also influence secondary phase formation differently. To assess the influence of annealing in spark plasma sintering (SPS) samples, Cheng *et al*. [52] investigated Co-doped β-$FeSi_2$ prepared under the same SPS conditions. They observed that secondary phases were formed in 8% Co-doped sample by SEM. By increasing the annealing time from 5 to 15 days and lowering the temperature from 900 °C to 750 °C, the secondary phases disappeared. These observations indicate that for both arc-melted and SPS-prepared samples, annealing is crucial to obtain a high-purity β-phase. Moreover, higher doping levels require optimized annealing conditions to suppress secondary phase formation.

III. Electrical transport improvement of β-$FeSi_2$-based materials

The conduction properties of β-$FeSi_2$ can be tuned to an n-type or p-type depending on the dopants. If Fe or Si is substituted with elements having fewer valence electrons (for example, Mn to the Fe site or Al to the Si site), the electrical conduction is p-type. In contrast, if they are substituted with elements having more valence electrons, the materials are changed to n-type. From the literature, **Table 1** and **Table 2**, respectively, list the electrical properties of n-type and p-type β-$FeSi_2$-based materials, including carrier density (n), mobility (μ), and the calculated electrical resistivity ($\rho = |e|^{-1}n^{-1}\mu^{-1}$, where e is the elementary charge constant). In **Table 1**, for n-type, Sam *et al.*[33] and Tani *et al.* [56] reported that the carrier density of Co-doped samples is about four orders of magnitude higher than that of pure β-$FeSi_2$. As a result, the ρ can be effectively reduced from ~ 10^0 to ~ 10^{-2} - 10^{-3} Ωcm, as the doping level increases from

0% to 6%. Importantly, Cheng *et al*. [52] attempted to increase the solid solution limits of Co atoms by prolonging the annealing time for 15 days. They obtained a high carrier density up to ~ 10^{22} cm^{-3} with solubility of Co up to 16%. On the other hand, by adding co-doping (Co + Ni), the mobility can be improved to 25 $cm^2V^{-1}s^{-1}$ because the substitution of Ni for Co probably modifies the electronic band structure, leading to a lighter effective mass [57]. Tani *et al*. found that, at the same doping level, the carrier density of Ni-doped samples is lower than that of Co-doped samples [56]. This is because Co atoms have a higher solubility in the β-$FeSi_2$ system than Ni atoms. The Pt element can also be used to tune the electrical properties of n-type β-$FeSi_2$. Importantly, the lowest electrical resistivity of ~ 10^{-4} Ωcm was obtained by 16% Ir doping [38]. This exceptional heavy doping led to a remarkable improvement in the *ZT* value of 0.6 due to the improvement of the power factor. **Table 2** summarizes the room temperature electrical properties of p-type β-$FeSi_2$ with Mn doping on the Fe site and Al doping on the Si site. The carrier density of Mn-doped samples can be enhanced to ~ 10^{18} - 10^{19} cm^{-3} as the doping level increases from 1% to 10% [44,51]. However, the higher carrier density of ~ 10^{20} cm^{-3} could be obtained by Al doping as reported by Du et al.[58]. Therefore, doping with Al is more effective in improving carrier density and electrical conductivity for β-$FeSi_2$.

It should be noted that for both n-type and p-type, mobility has an inverse tendency with carrier density or doping level. This relationship can be explained by the single parabolic band-acoustic phonon scattering model (SPB–APS model), which is commonly used to describe carrier transport in thermoelectric semiconductors. For example, the mobility decreases from 37 $cm^2V^{-1}s^{-1}$ to 1.9 $cm^2V^{-1}s^{-1}$ as Co doping

increases from 0% to 6% [33]. A similar tendency was also observed in Ni-doped samples as reported by Tani *et al*. [56]. The increase in both carrier density and mobility contributes to reducing electrical resistivity, leading to the enhancement of TE performance. A recent work attempted to improve the mobility of the Co-doped sample with Ni substitution [57]. Although the mobility was improved to 25 $cm^2V^{-1}s^{-1}$ with the addition of Ni, the Seebeck coefficient degraded due to the increase in the metallic phase. Therefore, the investigation of the phase fraction and microstructure evolutions is also important to understand the dopants' solubility, as it is related to improvement in carrier density and mobility.

IV. Thermoelectric properties of β-$FeSi_2$-based materials

A. Power factor improvement strategy

Power factor is one of the key parameters proportional to *ZT* value. The power factor is defined by: $PF = S^2\rho^{-1}$, where *S* is the Seebeck coefficient and ρ is the electrical resistivity. To improve the *PF* value, it is necessary to decrease ρ and increase *S*. **Fig. 6** illustrates the typical mechanism of transport properties improvement in β-$FeSi_2$ with the addition of dopants. Due to low carrier density (~ 10^{16} - 10^{17} cm^{-3}) [33,56], the ρ value of pure β-$FeSi_2$ is higher than that of other conventional TE materials. The reduction in ρ can be effectively obtained by increasing carrier density with elemental doping (**Fig. 6a**). Doping not only decreases ρ but also stabilizes *S* in the high-temperature region due to the reduction of bipolar effect. **Fig. 6b** shows the schematic of improving *S* by the doping approach. As mentioned in the Introduction section (**Fig. 2**), the narrow bandgap and low carrier density cause the decrease in *S* at high temperatures because of bipolar diffusion. This bipolar effect can be reduced by

increasing carrier density with doping. Therefore, doping can simultaneously improve *S* and decrease ρ. As a result, as shown in **Fig. 6c**, the thermoelectric power factor of β-$FeSi_2$ is remarkably improved via the doping technique.

Although doping significantly improves the *PF*, the doping levels should be optimized. There are two problems to be considered, such as solution limits and the trade-off relationship between carrier density and Seebeck coefficient according to Mott's theory. When the dopants reach their solubility limits, the secondary metallic phases form, and the Seebeck coefficient consequently decreases [51]. In addition, the inverse relation between carrier density and Seebeck coefficient is defined by Mott's formula [59]:

$$|S| = \frac{k_B^2 T}{3|e|\hbar^2} m^* \left(\frac{\pi}{3n}\right)^{2/3} \quad (1)$$

where $|S|$ is the absolute Seebeck coefficient, k_B is the Boltzmann constant, T is the temperature, $\hbar$ is the Planck constant, e is the elementary charge, m^* is the effective mass, and n is the carrier density. From **Eq. (1)**, if the carrier density increases too high due to high doping levels, the Seebeck coefficient decreases. Based on the theoretical calculation reported by Pandey *et al*. [60], the optimum carrier density for enhancing β-$FeSi_2$ performance is in range from 3×10^{20} to 2×10^{21} cm^{-3}. However, experimental optimization of the doping level is also necessary for improving the power factor of β-$FeSi_2$.

An experimental study of the optimization of the Mn doping level for p-type β-$FeSi_2$ has been conducted [51]. Based on the fraction analysis by Reitveld refinement, the amount of β-phase could be maintained at 95% for Mn doping levels of $\leq$ 8%.

However, the elemental mapping analysis by SEM-EDS indicates that the Mn reaches its solid solution limit in the β-phase at 5% Mn doping [44]. This suggests that the optimum Mn doping level should be lower than 5%. **Fig. 7** illustrates the variation in transport properties of β-$Fe_{1-x}Mn_xSi_2$ ($0 \leq x \leq 0.05$). In **Fig. 7a**, the electrical resistivity of all samples decreases with increasing temperature, indicating the semiconducting behavior over the measured temperature range from 80 K to 800 K. Notably, the resistivity of Mn-doped samples is about two orders of magnitude lower than that of the non-doped sample, and the resistivity continues to decrease with Mn doping level. As for the Seebeck coefficient, Mn doping tunes the conduction properties of β-$FeSi_2$ from n-type to p-type (**Fig. 7b**). The Seebeck coefficient for the $x = 0$ sample decreases with increasing temperature in the high-temperature region due to the bipolar diffusion effect. With the addition of Mn, the Seebeck coefficient is improved due to the suppression of the bipolar effect when the carrier density is optimized. However, for $x \geq 0.05$, the Seebeck coefficient decreases with increasing x because of the increased carrier density, as explained by Mott's theory. The relationship between the Seebeck coefficient, carrier density, and effective mass can be understood from **Fig. 7c**. For $0 \leq x \leq 0.04$, the Seebeck coefficient increases with increasing doping level due to the increase in effective mass m^* from 0.01 m_e to 1.53 m_e. The m^* was estimated using the Mott relation under the parabolic-band approximation, which is equivalent to the single parabolic band (SPB) model. However, the large variation in m^* suggests that this simplified model may not fully capture the non-parabolic and multivalley nature of Mn-doped β-$FeSi_2$. On the other hand, for $x \geq 0.04$, as the carrier density increases, the Seebeck coefficient then decreases with doping level. As a result, the maximum power factor PF = 970 $\mu Wm^{-1}K^{-2}$ at 800 K was obtained at the optimum doping level of 3%

Mn, as shown in **Fig. 7d**. Such a value is much higher than that of the non-doped sample (*PF* = 3.4 $\mu Wm^{-1}K^{-2}$). Du *et al*. [58] investigated another p-type material by Al doping on the Si site of β-$FeSi_{2-x}Al_x$ (x = 0.02, 0.03, and 0.04). Similar to the Mn-doped samples, the Seebeck coefficient of Al-doped samples was improved, and the electrical resistivity was effectively reduced with Al doping levels. As a result, the highest *PF* of 1100 $\mu Wm^{-1}K^{-2}$ at 500 K - 600 K was obtained in an Al doping level of x = 0.04 [58]. Komabayashi *et al*.[61] reported that the improvement in *PF* can also be obtained by Cr and V doping, with the *PF* value of 260 $\mu Wm^{-1}K^{-2}$ and 230 $\mu Wm^{-1}K^{-2}$ at room temperature, respectively.

For n-type β-$FeSi_2$, the improvement in the *PF* can be obtained by doping with Pt [61,62], Pd [61], Ni [53], Co [52,63–65], and Ir [38]. For example, at room temperature, the addition of Pt and Pd contributes to the *PF* enhancement of 190 $\mu Wm^{-1}K^{-2}$ and 490 $\mu Wm^{-1}K^{-2}$, respectively [61]. The addition of Ir also improves *PF* = 1800 $\mu Wm^{-1}K^{-2}$ at 1000 K. This improvement is mainly due to the reduction of electrical resistivity. Recently, our group investigated the effects of Ni doping (0.5% - 3.0%) on the TE properties of β-$FeSi_2$, and the maximum *PF* of 200 $\mu Wm^{-1}K^{-2}$ was obtained at a very low doping concentration of 0.5% Ni [53]. This indicates that Ni has a low solubility in β-$FeSi_2$. In addition, Tani *et al*. reported the TE properties of Co-doped samples, where the doping levels are from 1 % to 10%. They obtained the highest *PF* value of 1100 $\mu Wm^{-1}K^{-2}$ in the 5% Co-doped sample. This value is in agreement with that reported by Birkholz *et al*. [66]. However, the *PF* value decreased when increasing Co doping up to 10% due to a reduction in the Seebeck coefficient. The

reduction in the Seebeck coefficient could probably be caused by its inverse relationship with the carrier density or due to the increase in the metallic phase. To solve this problem, Cheng *et al*. [52] attempted to improve the solubility of Co by optimizing the annealing conditions. As a result, they obtained a high solubility of 8% Co in β-$FeSi_2$ by increasing the annealing time to 15 days. Such a high solubility contributed to the *PF* enhancement of 1400 $\mu Wm^{-1}K^{-2}$ at 900 K. This indicates that optimizing the annealing condition improves the solid solution of dopants, contributing to *PF* enhancement. It should be noted that different dopants contribute to different levels of *PF* improvement. This is because of their solid solution limit levels, while improving the solubility of dopants significantly improves the *PF* value of the β-$FeSi_2$-based materials.

B. Thermal conductivity reduction strategy

The reduction in thermal conductivity is necessary because it has an inverse relation to the *ZT* value. The total thermal conductivity is dominated by the lattice and electronic part ($\kappa_{total} = \kappa_{lattice} + \kappa_{electronic}$). In semiconducting β-$FeSi_2$, the $\kappa_{lattice}$ is more dominant than $\kappa_{electronic}$, where major of the heat is transported by phonons. Therefore, the κ_{total} of β-$FeSi_2$ can be reduced by nanostructuring techniques and doping with heavy elements. Abbassi *et al*. [67] attempted to reduce the κ_{total} using nanostructures by the milling process. As shown in **Fig. 8a**, they found that the crystallite size decreases with increasing milling time, while the microstrain increases. As a result, the thermal conductivity of nano β-$FeSi_2$ (fabricated by ball milling techniques) is remarkably lower than the annealed one, as shown in **Fig. 8b**. The reduction of thermal conductivity upon ball milling is primarily attributed to enhanced phonon scattering at grain boundaries, which effectively suppresses the transport of heat-carrying phonons. The ball milling

process refines the grains, increases the density of grain boundaries, and introduces additional structural defects, all of which act as strong phonon scattering centers. Although minor lattice disorder (lattice softening) may also occur, its contribution is secondary compared to grain boundary scattering. The relationship between $\kappa_{lattice}$, τ, and υ_g can be expressed by: $\kappa_{lattice} = (1/3)\ C_v \upsilon_g^2 \tau = (1/3)\ C_v \upsilon_g l$, where C_v is the specific heat at constant volume, and l is the phonon mean free path [3]. Therefore, the decrease in τ due to phonon scattering at small crystallite size and the decrease in υ_g due to lattice softening caused by strain contribute to the reduction in $\kappa_{lattice}$ and κ_{total}. In addition, Le Tonquess *et al*. [68] introduced the stacking fault into pure β-$FeSi_2$ and Co-doped β-$FeSi_2$ synthesized by the magnesioreduction (MR) process. They found that the stacking probabilities of MR samples (*SF* = 10.7(2) % for pure β-$FeSi_2$ and *SF* = 10.4(1) % for Co-doped β-$FeSi_2$) were higher than that of arc-melted samples (*SF* = 3.7(1) % for pure β-$FeSi_2$ and *SF* = 3.2(1) % for Co-doped β-$FeSi_2$). As a result, the $\kappa_{lattice}$ of the pure sample and the Co-doped sample, respectively, decreases by 24 % and 17 % compared to that of the arc-melted samples. This reduction is attributed to the enhanced phonon scattering at the stacking faults. However, the electrical resistivity also increases in MR samples. This could be because of the decrease in mobility when electrons scatter more frequently at the stacking fault. In addition, Isoda *et al*. [15] investigated the effect of grain size on the κ_{total} for both p-type Mn-doped and n-type Co-doped β-$FeSi_2$ prepared by the ball milling process. For both p-type and n-type samples, the κ_{total} and with decreasing grain size from 24 μm to 11 μm and from 10 μm to 7 μm, respectively. This is mainly because of the decrease in $\kappa_{lattice}$, while the phonons are scattered by the grain boundaries. However, the electrical resistivity in the p-type sample increases with decreasing grain size (more boundaries are formed), which has a trade-off relationship

with κ_{total}. This phenomenon is similar when the stacking faults were introduced to β-$FeSi_2$ [68,69]. This indicates that the optimization of grain size, stacking fault, and crystallite size is necessary to selectively scatter the phonons while preserving the electron transport. This is about balancing the characteristic size of the structure in relation to the phonon and electron mean free path (MFP). It was reported that the non-doped β-$FeSi_2$ thin film and nanowire have the MFP of several hundred nanometers [70,71], while the electron MFP of ferromagnetic material ($FeSi_2$ can be ferromagnetic at the nanoscale) is only several nanometers [72,73]. However, the MFP values of phonon and electron at the bulk scale or when the dopants are added, can be different from those in the non-doped or thin film structures. Therefore, this is the opportunity for future research to conduct experimental or theoretical studies on the variation of electron and phonon MFP in the metal-doped β-$FeSi_2$ system. This could help us to understand the electro-thermal transport behavior and to design the characteristic sizes of the structure to balance the trade-off relationship between electrical and thermal conductivity toward enhancing the performance of the materials.

Another strategy to reduce the κ_{total} of the β-$FeSi_2$ system is the introduction of heavy elements such as Ge [45,74,75], Ru [47], Os [58], and Ir [38]. For example, Sangwan *et al*. [45] investigated the effect of SiGe addition on the TE properties of Al-doped β-$FeSi_2$ (**Fig. 9**). The κ_{total} values remarkably decrease with increasing SiGe concentration (**Fig. 9a**). In this case, systems containing heavier element (Ge) is anticipated to have reduced thermal conductivity, since larger atomic mass generally leads to lower phonon frequencies, stronger optical–acoustic scattering, and slower sound velocities [76]. However, as shown in **Fig. 9b**, the electrical conductivity also

decreases because the introduction of heavier elements enhances electron–phonon scattering and increases the effective mass of charge carriers, which reduces their mobility. In addition, modifications in the band structure caused by heavier atoms further limit carrier transport, resulting in lower conductivity. In **Fig. 9c**, the Seebeck coefficient is improved because heavier elements increase the effective mass of charge carriers and modify the band structure, which enhances the energy dependence of carrier transport. In addition, stronger scattering effects could favor high-energy carriers, further boosting the Seebeck coefficient. However, when the addition of SiGe is higher than 12%, the Seebeck coefficient remarkably decreases at high temperature. This is probably because the metallic ε-phase increases with increasing Ge concentration, as the formation of the metallic phase in the β-$FeSi_2$ system is sensitive to dopant concentration. Prolonging the annealing time could contribute to maintaining the β-phase [52] and thus improving the Seebeck coefficient. As for *ZT* values (**Fig. 9d**), the maximum value of 0.19 was obtained in the 10% SiGe-added sample, which is higher than the non-SiGe-added sample (*ZT*~0.15). Moreover, Du *et al*. [47] examined the effect of Ru incorporation as a heavy element on the thermoelectric properties of n-type Co-doped β-$FeSi_2$. They found that Ru atoms are unevenly distributed, since their diffusion is limited during annealing at 1173 K. But Ru doping significantly lowers the lattice $\kappa_{lattice}$ by introducing mass and strain field fluctuations that scatter phonons, while its influence on electrical transport remains minor. As a result, a maximum *ZT* of 0.33 was achieved at 900 K in the 5% Ru-doped sample, representing a 27% improvement over the sample without Ru. They further attempted to reduce the thermal conductivity of p-type Al-doped β-$FeSi_2$ with Os substitution [58]. At an Os concentration of 20%, the $\kappa_{lattice}$ reached a minimum of 2.6 $Wm^{-1}K^{-1}$ at 900 K. Importantly, Os addition

caused only a minor reduction in the *PF*, leading to a maximum *ZT* of 0.35 at 850 K. Recently, Qiu *et al*. [38] reported that 16% Ir doping induces multi-valley electronic conduction and enhances phonon-electron scattering, resulting in a *ZT* of 0.6 at 1000 K. In the three studies above, the authors limited the Ru, Os, and Ir concentrations to 5%, 20%, and 16%, respectively, yet the maximum *ZT* values were achieved at these highest concentrations. This suggests that exploring higher Ru, Os, and Ir content is possible to achieve greater *ZT* values.

Table 3 and **Table 4**, respectively, summarize the ZT_{max} values of n-type and p-type β-$FeSi_2$ with various dopants using different fabrication techniques. The tables are listed in the order from low to high values of ZT_{max}. It should be noted that the conduction behavior of the non-doped β-$FeSi_2$ can be n-type or p-type depending on the purity of raw elements, i.e., Fe and Si. When the sample was prepared with 5N-purity of raw elements, it could be n-type materials. On the other hand, 4N-purity raw elements could produce p-type materials [15]. However, as shown in **Tables 3** and **4**, the ZT_{max} ~ 0.01 of both n-type and p-type samples is very low compared to those with additions of dopants. For example, for n-type β-$FeSi_2$-based materials, the maximum *ZT* of 0.3 and 0.6 can be obtained by Co and Ir doping, respectively (**Table 3**). Some oxide particles (SiO_2, TiO, and Y_2O_3) [77,78] and heavy elements (Ge and Ru) [45,47,74,75,79] were added to the Co-doped β-$FeSi_2$ to further reduce the $\kappa_{lattice}$. Therefore, the *ZT* value can be enhanced due to the simultaneous improvement of *PF* and reduction in κ. For p-type β-$FeSi_2$-based materials, the maximum *ZT* of 0.21 and 0.35 can be obtained by Mn and Al+Os doping, respectively (**Table 4**). It is noted that the ZT_{max} value of 0.35 for p-type is still lower than that for n-type (~ 0.6). The lower *ZT* values are primarily due to the

low solid solution limit of dopants. Therefore, improving dopant solubility could further improve the *ZT* values.

Regarding the band structure, Pandey *et al*. [60] reported that the n-type β-$FeSi_2$ outperforms the p-type due to fundamental differences in their electronic structures. The conduction band comprises multiple heavy, anisotropic pockets that provide high density of states favorable for thermoelectric performance, while the valence band contains a light band near the VBM that limits p-type thermopower. This band structure difference allows n-type doping to maintain high thermopower (>200 μVK^{-1}) over a wider carrier concentration range (3×10^{20} to 2×10^{22} cm^{-3}) with reduced susceptibility to bipolar conduction effects. These computational insights explain the experimental observations of higher *ZT* in n-type β-$FeSi_2$ and provide guidance for optimizing doping strategies.

The schematic of the band structure of non-doped, Co-doped, and Ir-doped β-$FeSi_2$ is illustrated in **Fig. 10**. The computational study predicted superior n-type performance in β-$FeSi_2$ at high carrier concentrations because the curvature in the conduction band is flatter, leading to a higher effective mass (**Fig. 10a**) [60]. However, a recent experimental work by Cheng *et al*. [52] reveals that the choice of dopant determines whether this potential is realized. The superior n-type performance stems from the favorable conduction band structure featuring multiple heavy valleys that provide high density of states, whereas p-type performance is limited by a light valence band that reduces thermopower at practical doping concentrations [60]. Heavy Co doping up to 24% was achieved, confirming the feasibility of high n-type carrier concentrations. However, the maximum *ZT* of 0.3 occurred at only 8% doping and did

not improve with further Co addition. This contrasts sharply with Ir-doped β-$FeSi_2$, which achieved ZT = 0.6 at 16% doping as reported by Qiu *et al*. [38]. The disparity stems from fundamental differences in how Co and Ir modify the electronic structure. Co introduces localized impurity bands below the conduction band minimum, leading to low-mobility hopping conduction at low doping and impurity band conduction at high doping (**Fig. 10b**). In contrast, Ir creates impurity bands above the CBM (**Fig. 10c**), preserving the beneficial multi-valley conduction character predicted by Pandey *et al*. [60]. This explains why merely achieving high carrier concentration is insufficient, as the dopant must also maintain or enhance access to the favorable intrinsic conduction bands for optimal thermoelectric performance.

It should be noted that the improvement in thermoelectric performance of β-$FeSi_2$-based materials is not solely due to carrier density optimization. Qiu *et al*. [38] reported that Ir doping markedly reduces the total thermal conductivity to 2.8 $Wm^{-1}K^{-1}$ for β-$Fe_{0.84}Ir_{0.16}Si_2$, which is about one-seventh of pristine β-$FeSi_2$. This is mainly due to strong phonon scattering from point defects and enhanced electron–phonon interactions at high carrier concentrations (10^{21}–10^{22} cm^{-3}). These combined scattering mechanisms significantly suppress the lattice thermal conductivity (κ_L). In addition, Du *et al*. [47,58] reported that doping with atoms having heavier atomic masses and larger atomic radius (e.g, Ru and Os) to the Fe site leads to mass and strain field fluctuation, resulting in the reduction in κ_L. Possible band convergence effects may further contribute to the improved thermoelectric performance of metal-doped β-$FeSi_2$.

V. Conclusions and prospects

In this review, we discussed structural transitions and strategies to enhance the thermoelectric performance of metal-doped iron silicide (β-$FeSi_2$) as an abundant and non-toxic compound. The formation of metallic secondary phases is highly sensitive to dopant type and concentration, and their presence often degrades thermoelectric transport. Electrical properties and power factor can be improved by doping elements with more valence electrons, while lattice thermal conductivity is effectively reduced through nanostructuring techniques (ball milling and stacking faults) and heavy element alloying (Ge, Ru, Os, and Ir). However, nanostructuring also introduces grain boundary scattering that lowers electrical conductivity, and excessive doping beyond solubility limits promotes metallic phase formation, reducing the Seebeck coefficient.

Currently, the highest *ZT* value of 0.6 is achieved in 16% Ir-doped β-$FeSi_2$, benefiting from its relatively high solubility limit, which enhances the power factor while lowering thermal conductivity. Further exploration of higher Ir concentrations, combined with optimized annealing conditions to stabilize the β-phase, may yield even higher *ZT* values. In addition, exploring higher concentrations of other heavy elements (Ru and Os) could possibly further enhance *ZT* due to the reduction in thermal conductivity. Other dopants, such as Co and Pt (n-type) and Mn and Al (p-type), are also promising to improve the power factor because of the enhancement of both electrical conductivity and Seebeck coefficient. Their higher solubility requires careful control of annealing temperature and duration to suppress secondary phase formation.

Hence, three major strategies are crucial: (i) enhancing dopant solubility, (ii) incorporating heavier elements to disrupt phonon transport, and (iii) designing nanostructures with controlled grain sizes and stacking faults. Importantly, predicting and tuning phonon and electron mean free paths will be essential for engineering

nanostructures that selectively scatter phonons while minimizing adverse effects on carrier mobility. Therefore, these approaches provide a pathway toward further improving the thermoelectric performance of β-$FeSi_2$ and establishing it as a sustainable thermoelectric material.

Author Contribution

S. Sam: Conceptualization, Data curation, Formal analysis, Investigation, Methodology, Writing – original draft, Writing – review & editing. **S. Say**: Data curation, Writing – review & editing. **K. Yamazaki**: Review & editing. **H. Nakatsugawa**: Writing – review & editing.

Declaration of Competing Interest

The authors declare that they have no known competing financial interests or personal relationships that could have appeared to influence the work reported in this paper.

ORCID

Sopheap Sam: https://orcid.org/0000-0001-5110-3446

Sreypich Say: https://orcid.org/0009-0005-1405-2455

Kosuke Yamazaki: https://orcid.org/0009-0003-5747-9024

Hiroshi Nakatsugawa: https://orcid.org/0000-0003-3971-939X

References

[1] Caballero-Calero O, Ares J R, and Martín-González M. Environmentally Friendly Thermoelectric Materials: High Performance from Inorganic Components with Low Toxicity and Abundance in the Earth. *Adv. Sustain. Syst.* 2021; **5**: 2100095. doi: 10.1002/adsu.202100095

[2] Song K, Tanvir A N M, Bappy M O, *et al*. New Directions for Thermoelectrics: A Roadmap from High-Throughput Materials Discovery to Advanced Device Manufacturing. *Small Sci.* 2024; **5**: 2300359. doi: 10.1002/smsc.202300359

[3] Takeuchi T. New Thermoelectric Materials with Precisely Determined Electronic Structure and Phonon Dispersion. *Thermoelectrics and its Energy Harvesting* ed D M Rowe (Taylor & Francis Group: Abingdon, UK), 2017, pp 7-1-7–27. doi: 10.1201/b11891

[4] Nakatsugawa H, Kubota M and Saito M. P-Type Thermoelectric Properties of $Pr_{1-x}Sr_xMnO_3$ ($0.1 \leq x \leq 0.3$) and $La_{1-x}Sr_xFeO_3$ ($0.1 \leq x \leq 0.3$). *J. Japan Inst. Met.* 2015; **79**: 597–606. doi: 10.2320/jinstmet.JA201516

[5] Nakatsugawa H, Saito M and Okamoto Y. High-Temperature Thermoelectric Properties of $Pr_{1-x}Sr_xFeO_3$ ($0.1 \leq x \leq 0.7$). *Mater. Trans.* 2019; **60**: 1051–60. doi: 10.2320/matertrans.E-M2019812

[6] Ohta H. Thin film growth and thermoelectric properties of electron conducting oxides. *J. Ceram. Soc. Japan* 2022; **130**: 22061. doi: 10.2109/jcersj2.22061

[7] Nakatsugawa H, Kamatani Y, Okamoto Y, *et al*. Crystal structure, magnetism, and thermoelectric properties of $Nd_{1-x}Sr_xFeO_{3-\delta}$ ($0.1 \leq x \leq 0.9$). *Jpn. J. Appl. Phys.* 2023; **62**: 043001. doi: 10.35848/1347-4065/acc9f3

[8] Zhu H, Li W, Nozariasbmarz A, *et al*. Half-Heusler alloys as emerging high power density thermoelectric cooling materials. *Nat. Commun.* 2023; **14**: 3300. doi: 10.1038/s41467-023-38446-0

[9] Difalco A, Winning I G, Palumbo M, *et al*. Transport properties of Co_2HfSn Heusler alloy obtained by rapid solidification and sintering. *Solid State Sci.* 2024; **149**: 107455. doi: 10.1016/j.solidstatesciences.2024.107455

[10] Yamazaki K, Sam S, Okamoto Y, *et al*. Tuning conduction properties and clarifying thermoelectric performance of P-type half-heusler alloys $TiNi_{1-x}Co$ Sn ($0 \leq x \leq 0.15$). *Solid State Sci.* 2024; **157**: 107708. doi: 10.1016/j.solidstatesciences.2024.107708

[11] Nakatsugawa H, Ozaki T, Kishimura H, *et al*. Thermoelectric Properties of Heusler Fe2TiSn Alloys. *J. Electron. Mater.* 2020; **49**: 2802. doi: 10.1007/s11664-019-07855-7

[12] Katsuyama S, Matsushima H and Ito M. Effect of substitution for Ni by Co and/or Cu on the thermoelectric properties of half-Heusler ZrNiSn. *J. Alloys Compd.* 2004; **385**: 232. doi: 10.1016/j.jallcom.2004.02.061

[13] Ai X, Lei B, Cichocka M O, *et al*. Enhancing the Thermoelectric Properties via Modulation of Defects in P-Type MNiSn-Based (M = Hf, Zr, Ti) Half-Heusler Materials. *Adv. Funct. Mater.* 2023; **33**: 2305582. doi: 10.1002/adfm.202305582

[14] Nogi K and Kita T. Rapid production of β-$FeSi_2$ by spark-plasma sintering. *J. Mater. Sci.* 2000; **35**: 5845. doi: https://doi.org/10.1023/A:1026752206864

[15] Isoda Y and Udono H. Preparation and Thermoelectric Properties of Iron Disilicide. *Thermoelectrics and its Energy Harvesting* ed D M Rowe (CRC Press) 2017, 18-1-18–25. doi: 10.1201/b11891

[16] Nozariasbmarz A, Agarwal A, Coutant Z A, *et al*. Thermoelectric silicides: A review. *Jpn. J. Appl. Phys.* 2017; **56**: 05DA04. doi: 10.7567/JJAP.56.05DA04

[17] Burkov A T. Silicide Thermoelectrics: Materials for Energy Harvesting. *Phys. status solidi* 2018; **215**: 1800105. doi: 10.1002/pssa.201800105

[18] Iida T, Inoue R, Shiojiri D, *et al*. Silicide materials: Thermoelectric, mechanical properties, and durability for Mg-Si and Mn-Si. *Thermoelectric Energy*

Conversion Woodhead Publishing Series in Electronic and Optical Materials, 2021, 389–427. doi: 10.1016/B978-0-12-818535-3.00030-X

[19] Kim G, Shin H, Lee J, *et al*. A Review on Silicide-Based Materials: Thermoelectric and Mechanical Properties. *Met. Mater. Int.* 2021; **27**: 2205–19. doi: 10.1007/s12540-020-00609-9

[20] Binti A, Liana F, Ahmad S, *et al*. A review on the effects of various elemental doping and nanostructuring of β-$FeSi_2$/Si_2 composites on the thermoelectric performance enhancement. *Mater. Today Proc.* 2022; **65**: 2979–85. doi: 10.1016/j.matpr.2022.03.150

[21] Saito T and Asakawa R. Production of (Fe, Co)Si_2 and (Fe, Mn)Si_2 Thermoelectric Materials by Spark Plasma Sintering. *Crystals* 2023; **14**: 56. doi: 10.3390/cryst14010056

[22] Priyanka and Muthiah S. Process-structure-properties relationship in low-cost thermoelectric iron silicide synthesis. *Ceram. Int.* 2022; **48**: 29366. doi: 10.1016/j.ceramint.2022.05.382

[23] Inoue H, Kobayashi T, Kato M, *et al*. A Low-Cost Production Method of $FeSi_2$ Power Generation Thermoelectric Modules. *J. Electron. Mater.* 2016; **45**: 1767–71. doi: 10.1007/s11664-015-4208-4

[24] Shibuya M, Kawata M, Shinohara Y, *et al*. Eco-Fabrication Process and Thermoelectric Properties of β-$FeSi_2$. *Trans. Mater. Res. Soc. Japan* 2015; **40**: 219. doi: 10.14723/tmrsj.40.219

[25] Cheng J, Chen X, Zhou J, *et al.* Crystal Structure and Chemical Bonding of β-$FeSi_2$ and ε-FeSi. *J. Phys. Chem. C* 2024; **128**: 13998–4006. doi: 10.1021/acs.jpcc.4c03032

[26] Sakata T, Sakai Y, Yoshino H, *et al*. Studies on the formation of $FeSi_2$ from the FeSi-Fe_2Si_5 eutectic. *J. Less Common Met.* 1978; **61**: 301. doi: 10.1016/0022-5088(78)90225-4

[27] Pauling L and Soldate A M. The nature of the bonds in the iron silicide, FeSi, and related crystals. *Acta Crystallogr.* 1948; **1**: 212. doi: 10.1107/S0365110X48000570

[28] Dusausoy Y, Protas J, Wandji R, *et al*. Structure cristalline du disiliciure de fer, β-$FeSi_2$. *Acta Crystallogr. Sect. B Struct. Crystallogr. Cryst. Chem.* 1971; **27**: 1209. doi: 10.1107/S0567740871003765

[29] Nishida I. Study of Semiconductor-to-Metal Transition in Mn-Doped $FeSi_2$. *Phys. Rev. B* 1973; **7**: 2710. doi: 10.1103/PhysRevB.7.2710

[30] Nishida I, Masumoto K, Okamoto M, *et al*. Formation of $FeSi_2$ from Sintered FeSi and Fe_2Si_5 Eutectic Alloy. *Trans. Japan Inst. Met.* 1985; **26**: 369. doi: 10.2320/matertrans1960.26.369

[31] Sales B C, Delaire O, McGuire M A, *et al*. Thermoelectric properties of Co-, Ir-, and Os-doped FeSi alloys: Evidence for strong electron-phonon coupling. *Phys. Rev. B* 2011; **83**: 125209. doi: 10.1103/PhysRevB.83.125209

[32] Clark S J, Al-Allak H M, Brand S, *et al*. Structure and electronic properties of $FeSi_2$. *Phys. Rev. B* 1998; **58**: 10389. doi: 10.1103/PhysRevB.58.10389

[33] Sam S, Nakatsugawa H, and Okamoto Y. Optimization of Co additive amount to improve thermoelectric properties of β-$FeSi_2$. *Jpn. J. Appl. Phys.* 2022; **61**: 111002. doi: 10.35848/1347-4065/ac96b7

[34] Bahk J-H and Shakouri A. Enhancing the thermoelectric figure of merit through the reduction of bipolar thermal conductivity with heterostructure barriers. *Appl.*

Phys. Lett. 2014; **105**: 052106. doi: 10.1063/1.4892653

[35] Gong J J, Hong A J, Shuai J, *et al*. Investigation of the bipolar effect in the thermoelectric material $CaMg_2Bi_2$ using a first-principles study. *Phys. Chem. Chem. Phys.* 2016; **18**: 16566–74. doi: 10.1039/C6CP02057G

[36] Chen Z, Zhang X, Ren J, *et al*. Leveraging bipolar effect to enhance transverse thermoelectricity in semimetal Mg_2Pb for cryogenic heat pumping. *Nat. Commun.* 2021; **12**: 3837. doi: 10.1038/s41467-021-24161-1

[37] Sam S, Yamazaki K, and Nakatsugawa H. Thermal conductivity reduction and crystal properties evolution in iron silicides induced by doping. *Solid State Commun.* 2024; **394**: 115700. doi: 10.1016/j.ssc.2024.115700

[38] Qiu P, Cheng J, Chai J, *et al*. Exceptionally Heavy Doping Boosts the Performance of Iron Silicide for Refractory Thermoelectrics. *Adv. Energy Mater.* 2022; **12**: 2200247. doi: 10.1002/aenm.202200247

[39] Yamazaki K, Sam S, and Nakatsugawa H. P-type thermoelectric properties of $TiNi_{1-x-y}Co_ySn$ half-Heusler alloy with reduced interstitial Ni atoms. *Solid State Sci.* 2025; **169**: 108060. doi: 10.1016/j.solidstatesciences.2025.108060

[40] Zhang X, Zhang Y, Wu L, *et al*. $Ba_{1/3}CoO_2$: A Thermoelectric Oxide Showing a Reliable ZT of ~0.55 at 600 °C in Air. *ACS Appl. Mater. Interfaces* 2022; **14**: 33355–60. doi: 10.1021/acsami.2c08555

[41] Nakatsugawa H, Saito M, and Okamoto Y. High-Temperature Thermoelectric Properties of Perovskite-Type $Pr_{0.9}Sr_{0.1}Mn_{1-x}Fe_xO_3$ ($0 \leq x \leq 1$). *J. Electron. Mater.* 2017; **46**: 3262–72. doi: 10.1007/s11664-017-5366-3

[42] Fukutomi H, Konno Y, Okayasu K, *et al*. Texture development of $Ca_3Co_4O_9$ thermoelectric oxide by high temperature plastic deformation and its contribution

to the improvement in electric conductivity. *Mater. Sci. Eng. A* 2009; **527**: 61–4. doi: 10.1016/j.msea.2009.08.012

[43] Sam S, Yamazaki K and Nakatsugawa H. Investigation of phase fraction in α-Fe_2Si_5, ε-FeSi, and β-$FeSi_2$ thermoelectric materials doped with Co and Ni. *Solid State Commun.* 2023; **371**: 115287. doi: 10.1016/j.ssc.2023.115287

[44] Sam S, Farooq U, Namba M, *et al*. Structure relations with transport properties in p-type thermoelectric materials: Iron silicides. *J. Alloys Compd.* 2024; **989**: 174367. doi: 10.1016/j.jallcom.2024.174367

[45] Sangwan P, Upadhyay N K, Shyam R, *et al*. Hybrid composite approach enhancing the thermoelectric performance of p-type iron-silicide synthesized by the arc melting-spark plasma sintering technique. *Hybrid Adv.* 2025; **9**: 100423. doi: 10.1016/j.hybadv.2025.100423

[46] Ito M, Nagai H, Tanaka T, *et al*. Thermoelectric performance of n-type and p-type β-$FeSi_2$ prepared by pressureless sintering with Cu addition. *J. Alloys Compd.* 2001; **319**: 303–11. doi: 10.1016/S0925-8388(01)00920-3

[47] Du X, Hu P, Mao T, *et al*. Ru Alloying Induced Enhanced Thermoelectric Performance in $FeSi_2$-Based Compounds. *ACS Appl. Mater. Interfaces* 2019; **11**: 32151–8. doi: 10.1021/acsami.9b10648

[48] P. Klug H and E. Alexander L. X-Ray Diffraction Procedure. (John Wiley &Sons Inc., New York) pp 491–538

[49] Jeffery G A. Elements of x-ray diffraction (Cullity, B. D.). *J. Chem. Educ.* 1957; **34**: A178. doi: 10.1021/ed034pA178

[50] Kojima T, Masumoto K, Okamoto M, *et al*. Formation of β-$FeSi_2$ from the sintered eutectic alloy FeSi-Fe_2Si_5 doped with cobalt. *J. Less Common Met.*

1990; **159**: 299–305. doi: 10.1016/0022-5088(90)90157-F

[51] Sam S, Farooq U, Oshita R, *et al*. Insight into phase stability and thermoelectric properties of semiconducting iron silicides with manganese substitution: β-$Fe_{1-x}Mn_xSi_2$ ($0 \leq x \leq 0.05$). *J. Phys. Chem. Solids* 2024; **194**: 112224. doi: 10.1016/j.jpcs.2024.112224

[52] Cheng J, Gan L, Zhang J, *et al*. Thermoelectric properties of heavily Co-doped β-$FeSi_2$. *J. Mater. Sci. Technol.* 2024; **187**: 248–57. doi: 10.1016/j.jmst.2023.11.039

[53] Sam S, Odagawa S, Nakatsugawa H, *et al*. Effect of Ni Substitution on Thermoelectric Properties of Bulk β-$Fe_{1-x}Ni_xSi2$ ($0 \leq x \leq 0.03$). *Materials.* 2023; **16**: 927. doi: 10.3390/ma16030927

[54] Dąbrowski F, Ciupiński Ł, Zdunek J, *et al*. Microstructure and thermoelectric properties of p and n-type doped β-$FeSi_2$ fabricated by mechanical alloying and pulse plasma sintering. *Mater. Today Proc.* 2019; **8**: 531–9. doi: 10.1016/j.matpr.2019.02.050

[55] Dąbrowski F, Ciupiński, Zdunek J, *et al*. Microstructure and Thermoelectric Properties of Doped $FeSi_2$ With Addition of B_4C Nanoparticles. *Arch. Metall. Mater.* 2021; **66**: 1157. doi: 10.24425/amm.2021.136436

[56] Tani J and Kido H. Electrical properties of Co-doped and Ni-doped β-$FeSi_2$. *J. Appl. Phys.* 1998; **84**: 1408. doi: 10.1063/1.368174

[57] Sam S, Nakatsugawa H, and Okamoto Y. Improved thermoelectric performance of Co-doped β-$FeSi_2$ by Ni substitution. *Mater. Adv.* 2023; **4**: 2821. doi: 10.1039/D3MA00153A

[58] Du X, Qiu P, Chai J, *et al*. Doubled Thermoelectric Figure of Merit in p-Type β-

$FeSi_2$ via Synergistically Optimizing Electrical and Thermal Transports. *ACS Appl. Mater. Interfaces* 2020; **12**: 12901. doi: 10.1021/acsami.0c00321

[59] Mott N F. Conduction in glasses containing transition metal ions. *J. Non. Cryst. Solids* 1968; **1**: 1–17. doi: 10.1016/0022-3093(68)90002-1

[60] Pandey T, Singh D J, Parker D, *et al*. Thermoelectric properties of β-$FeSi_2$. *J. Appl. Phys.* 2013; **114**: 153704. doi: 10.1063/1.4825217

[61] Komabayashi M and Ido K H. Effects of Some Additives on Thermoelectric Properties of $FeSi_2$ Thin Films. *Jpn. J. Appl. Phys.* 1991; **30**: 331. doi: 10.1143/JJAP.30.331

[62] Tani J and Kido H. Thermoelectric properties of Pt-doped β-$FeSi_2$. *J. Appl. Phys.* 2000; **88**: 5810. doi: 10.1063/1.1322597

[63] Tani J and Kido H. Thermoelectric Properties of β-$Fe_{1-x}Co_xSi_2$ Semiconductors. *Jpn. J. Appl. Phys.* 2001; **40**: 3236. doi: 10.1143/JJAP.40.3236

[64] Ito M, Tada T, and Katsuyama S. Thermoelectric properties of $Fe_{0.98}Co_{0.02}Si_2$ with ZrO_2 and rare-earth oxide dispersion by mechanical alloying. *J. Alloys Compd.* 2003; **350**: 296–302. doi: 10.1016/S0925-8388(02)00964-7

[65] Yamashita O, Tomiyoshi S, and Sadatomi N. Thermoelectric properties of p- and n-type $FeSi_2$ prepared by spray drying, compaction and sintering technique. *J. Mater. Sci.* 2003; **38**: 1623. doi: 10.1023/A:1023251004461

[66] Birkholz U and Schelm J. Mechanism of Electrical Conduction in β-$FeSi_2$. *Phys. status solidi* 1968; **27**: 413. doi: 10.1002/pssb.19680270141

[67] Abbassi L, Mesguich D, Berthebaud D, *et al*. Effect of Nanostructuring on the Thermoelectric Properties of β-$FeSi_2$. *Nanomaterials* 2021; **11**: 2852. doi: 10.3390/nano11112852

[68] Le Tonquesse S, Verastegui Z, Huynh H, *et al.* Magnesioreduction Synthesis of Co-Doped β-$FeSi_2$: Mechanism, Microstructure, and Improved Thermoelectric Properties. *ACS Appl. Energy Mater.* 2019; **2**: 8525. doi: 10.1021/acsaem.9b01426

[69] Yamane H and Yamada T. Effects of stacking fault on the diffraction intensities of β-$FeSi_2$. *J. Alloys Compd.* 2009; **476**: 282. doi: 10.1016/j.jallcom.2008.08.078

[70] Ail U, Gorsse S, Perumal S, *et al*. Thermal conductivity of β-$FeSi_2$/Si endogenous composites formed by the eutectoid decomposition of α-Fe2Si5. *J. Mater. Sci.* 2015; **50**: 6713. doi: 10.1007/s10853-015-9225-4

[71] Hsin C-L, Liu Y-T and Tsai Y-Y. Suppressed Umklapp scattering of β-$FeSi_2$ thin film and single crystalline nanowires. *Nanotechnology* 2017; **28**: 485702. doi: 10.1088/1361-6528/aa904a

[72] Gurney B A, Speriosu V S, Nozieres J-P, *et al*. Direct measurement of spin-dependent conduction-electron mean free paths in ferromagnetic metals. *Phys. Rev. Lett.* 1993; **71**: 4023. doi: 10.1103/PhysRevLett.71.4023

[73] Yoshitake T, Ogawa T, Nakagauchi D, *et al*. Interlayer coupling in ferromagnetic epitaxial $Fe_3Si/FeSi_2$ superlattices. *Appl. Phys. Lett.* 2006; **89**: 23. doi: 10.1063/1.2410222

[74] Liu N, Jensen W A, Zebarjadi M, *et al*. Tunable β-$FeSi_2$– $Si_{1-y}Ge_y$ nanocomposites by a novel React/Transform Spark Plasma Sintering approach for thermoelectric applications. *Mater. Today Phys.* 2018; **4**: 19–27. doi: 10.1016/j.mtphys.2018.02.004

[75] Liu N, Rezaei S E, Jensen W A, *et al*. Improved Thermoelectric Performance of Eco-Friendly β-$FeSi_2$–SiGe Nanocomposite via Synergistic Hierarchical

Structuring, Phase Percolation, and Selective Doping. *Adv. Funct. Mater.* 2019; **29**: 1903157. doi: 10.1002/adfm.201903157

[76] Saha S K. Exploring the origin of ultralow thermal conductivity in layered BiOCuSe. *Phys. Rev. B* 2015; **92**: 041202. doi: 10.1103/PhysRevB.92.041202

[77] Ito M, Tada T, and Hara S. Effects of $Y2O_3$ and Y Addition on Thermoelectric Properties of β-$FeSi_2$ Synthesized by Mechanical Alloying and Hot Pressing. *Mater. Trans.* 2004; **45**: 2916. doi: 10.2320/matertrans.45.2916

[78] Ito M, Tanaka T, and Hara S. Thermoelectric properties of β-$FeSi_2$ with electrically insulating SiO2 and conductive TiO dispersion by mechanical alloying. *J. Appl. Phys.* 2004; **95**: 6209. doi: 10.1063/1.1710725

[79] Kim S W, Cho M K, Mishima Y, *et al*. High temperature thermoelectric properties of p- and n-type β-$FeSi_2$ with some dopants. *Intermetallics* 2003; **11**: 399–405. doi: 10.1016/S0966-9795(03)00020-7

[80] Brehme S, Behr G and Heinrich A. Electrical properties of Co-doped β-$FeSi_2$ crystals. *J. Appl. Phys.* 2001; **89**: 3798–803. doi: 10.1063/1.1350996

[81] Ito M, Nagai H, Oda E, *et al*. Effects of P doping on the thermoelectric properties of β-$FeSi_2$. *J. Appl. Phys.* 2002; **91**: 2138. doi: 10.1063/1.1436302

[82] Soon-Chul Ur. Mechanical alloying and thermoelectric properties of Co-doped $FeSi_2$. *Proceedings ICT'03. 22nd International Conference on Thermoelectrics (IEEE Cat. No.03TH8726)* 2003 (IEEE) 149–52. doi: 10.1109/ICT.2003.1287471

[83] Redzuan M, Mikio I, and Masatoshi T. Synthesis of Co-doped β-$FeSi_2$/Si composites through eutectoid decomposition and its thermoelectric properties. *J. Mater. Sci.* 2018; **53**: 7683. doi: 10.1007/s10853-018-2066-1

[84] He Z, Platzek D, Stiewe C, *et al*. Thermoelectric properties of hot-pressed Al-

and Co-doped iron disilicide materials. *J. Alloys Compd.* 2007; **438**: 303. doi: 10.1016/j.jallcom.2006.08.045

[85] Kimura Y, Yamada M and Chai Y W. Thermoelectric Properties of Nearly Single-Phase β-$FeSi_2$ Alloys Fabricated by Gas-Atomized Powder Sintering. *Mater. Trans.* 2019; **60**: 652. doi: 10.2320/matertrans.MB201805

[86] Chen H Y, Zhao X B, Stiewe C, *et al.* Microstructures and thermoelectric properties of Co-doped iron disilicides prepared by rapid solidification and hot pressing. *J. Alloys Compd.* 2007; **433**: 338. doi: 10.1016/j.jallcom.2006.06.080

[87] Tani J and Kido H. Thermoelectric Properties of Mn-Doped β-$FeSi_2$ Fabricated by Spark Plasma Sintering. *J. Ceram. Soc. Japan* 2001; **109**: 557. doi: 10.2109/jcersj.109.1270_557

List of Figures

Fig. 1 Three-dimensional crystal structures of iron silicide. The left and middle panels are metallic phases, the tetragonal α-phase and cubic ε-phase. The right panel is the structure of the semiconducting β-phase.

Fig. 2 (a) A schematic explains the mechanism of the bipolar effect that occurs at high temperatures for low carrier density semiconductors, resulting in a significant reduction in Seebeck coefficient. **(b)** The increase in electron density contributes to the reduction in the bipolar effect at high temperatures, resulting in an improvement in the Seebeck coefficient.

Fig. 3 Rietveld refinement of the X-ray diffraction data of **(a)** non-doped $FeSi_2$, **(b)** with 10%Co doping, and **(c)** with 10% Mn doping. The index peaks are the peaks of the

semiconducting β-phase. The arrows indicate the peaks of impurity phases (ε and α-phases). Reproduced from the Ref. [43] © *Elsevier 2023*, and Ref. [44] © *Elsevier 2024.*

Fig. 4 (a) The variation of β-phase and **(b)** *a*-lattice constant dependence of the doping levels of Mn, Co, and Ni obtained by the Rietveld analysis. The data plotted in this figure are collected from Refs. [43,44,51].

Fig. 5 SEM-EDS mapping to observe the variation in microstructure of Ni-doped β-$FeSi_2$. The Ni doping level is from 0.5% to 3%. The Fe elements are mapped in red, Ni in green, and Si in blue. Reproduced from Ref. [53] © *2023 by the authors, licensed under CC BY 4.0* (https://creativecommons.org/licenses/by/4.0/)

Fig. 6. Schematic illustration of the transport properties improvement of β-$FeSi_2$ with doping. **(a)** Decrease in electrical resistivity (ρ), **(b)** Improvement of Seebeck coefficient (S) at high temperature region, and **(c)** Enhancement in power factor ($PF = S^2\rho^{-1}$).

Fig. 7. Transport properties of β-$Fe_{1-x}Mn_xSi_2$ ($0 \leq x \leq 0.05$). **(a)** Temperature dependence of electrical resistivity ρ, and **(b)** Seebeck coefficient S. **(c)** Seebeck coefficient vs. carrier density at room temperature. The solid lines are the calculated data from the Mott formula in **Eq. (1)** at various effective masses $m^* = xm_e$, where x is a variable and m_e is the static mass of the electron, i.e., 9.10938×10^{-31} kg. The blue arrow indicates that the Seebeck coefficient increases with doping level due to the increase in effective mass, while the red arrow indicates the Seebeck coefficient decreases with increasing carrier density. **(d)** Temperature dependence of power factor *PF*. Reproduced from Ref. [51]. © *Elsevier 2024.*

Fig. 8. The result of thermal conductivity reduction by nanostructuring with the milling process. **(a)** The crystallite size as a function of ball milling time (left axis) and micro-strain on the right axis. **(b)** The temperature dependence of the thermal conductivity of annealed β-$FeSi_2$ and nano β-$FeSi_2$ (fabricated by ball milling techniques). Reproduced

from Ref. [67]. © *2021 by the authors, licensed under CC BY 4.0* (https://creativecommons.org/licenses/by/4.0/).

Fig. 9. Improved thermoelectric performance by reducing thermal conductivity of Al-doped β-$FeSi_2$ with the addition of Ge as a heavy element. **(a)** Total thermal conductivity, **(b)** electrical conductivity, **(c)** Seebeck coefficient, and **(d)** *ZT* values with temperature dependence. Reproduced from Ref. [45]. © *2025 by the authors, under the CC BY license* (http://creativecommons.org/licenses/by/4.0/)

Fig. 10. Schematic of the band structure of **(a)** non-doped, **(b)** Co-doped, and **(c)** Ir-doped β-$FeSi_2$.

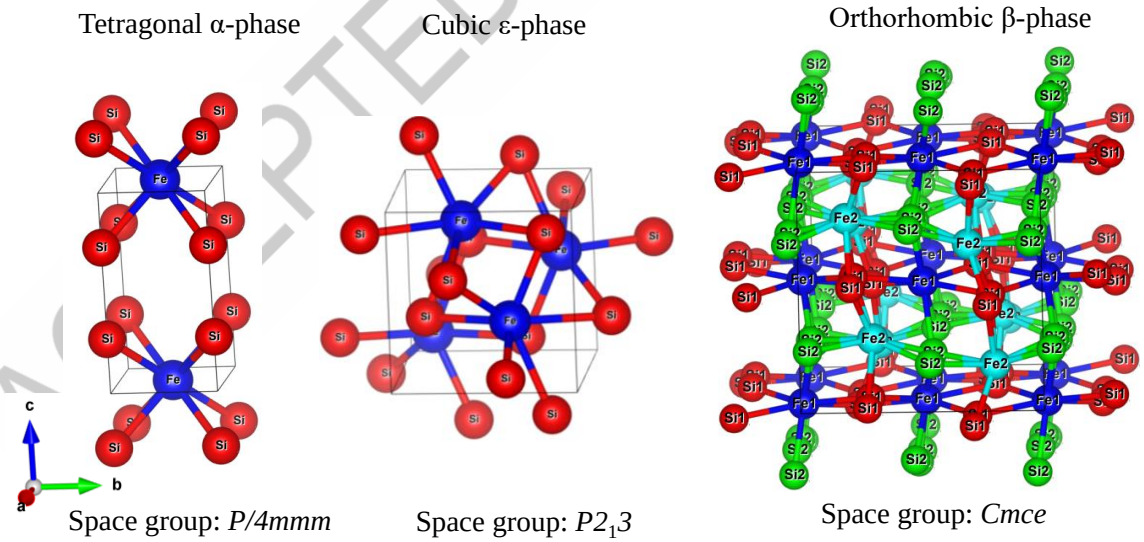

Fig. 1 Three-dimensional crystal structures of iron silicide. The left and middle panels are metallic phases, the tetragonal α-phase and cubic ε-phase. The right panel is the structure of the semiconducting β-phase.

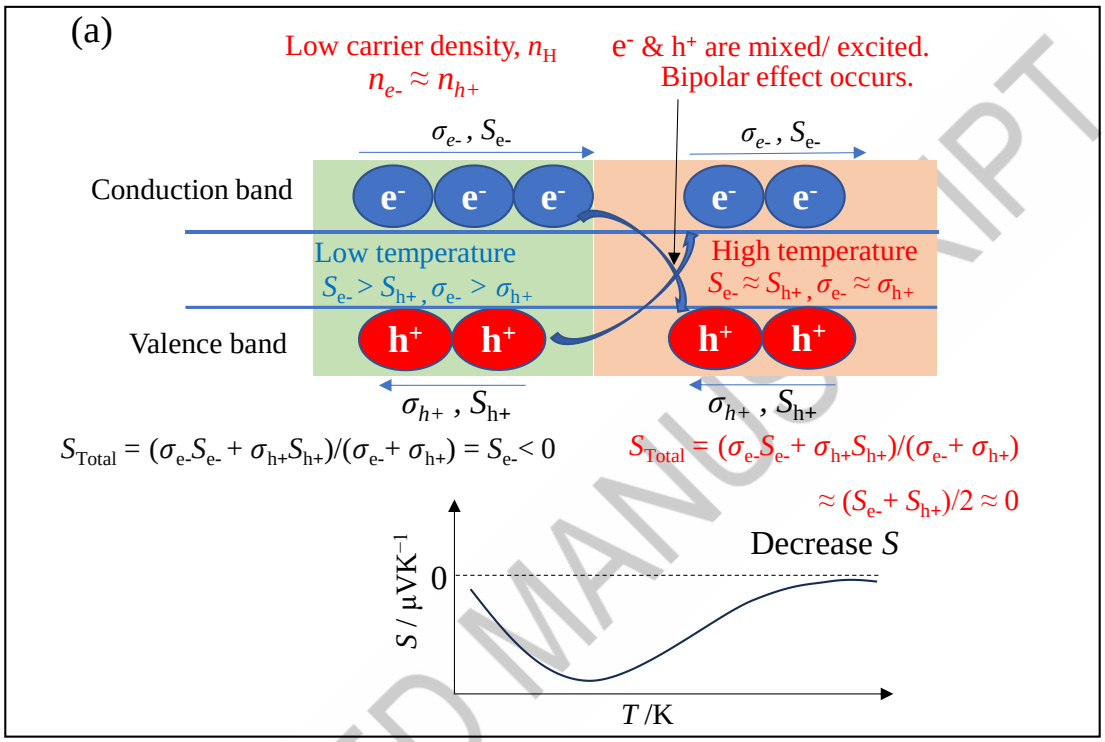

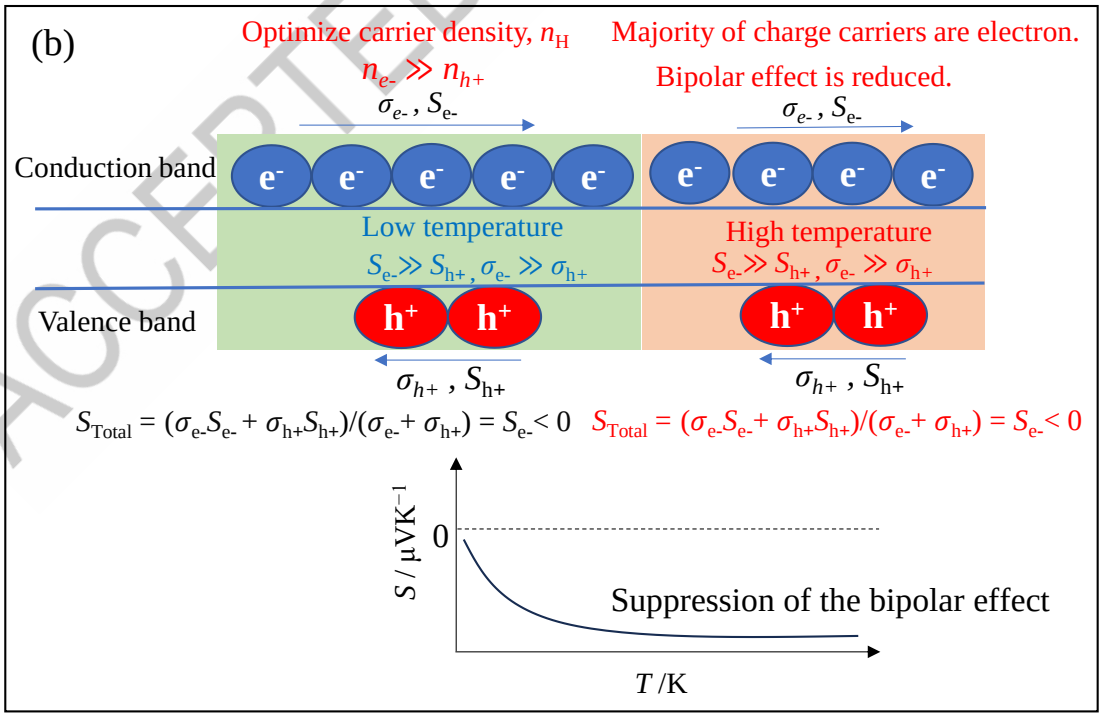

Fig. 2 (a) A schematic explains the mechanism of the bipolar effect that occurs at high temperatures for low carrier density semiconductors, resulting in a significant reduction in Seebeck coefficient. **(b)** The increase in electron density contributes to the reduction in the bipolar effect at high temperatures, resulting in an improvement in the Seebeck coefficient.

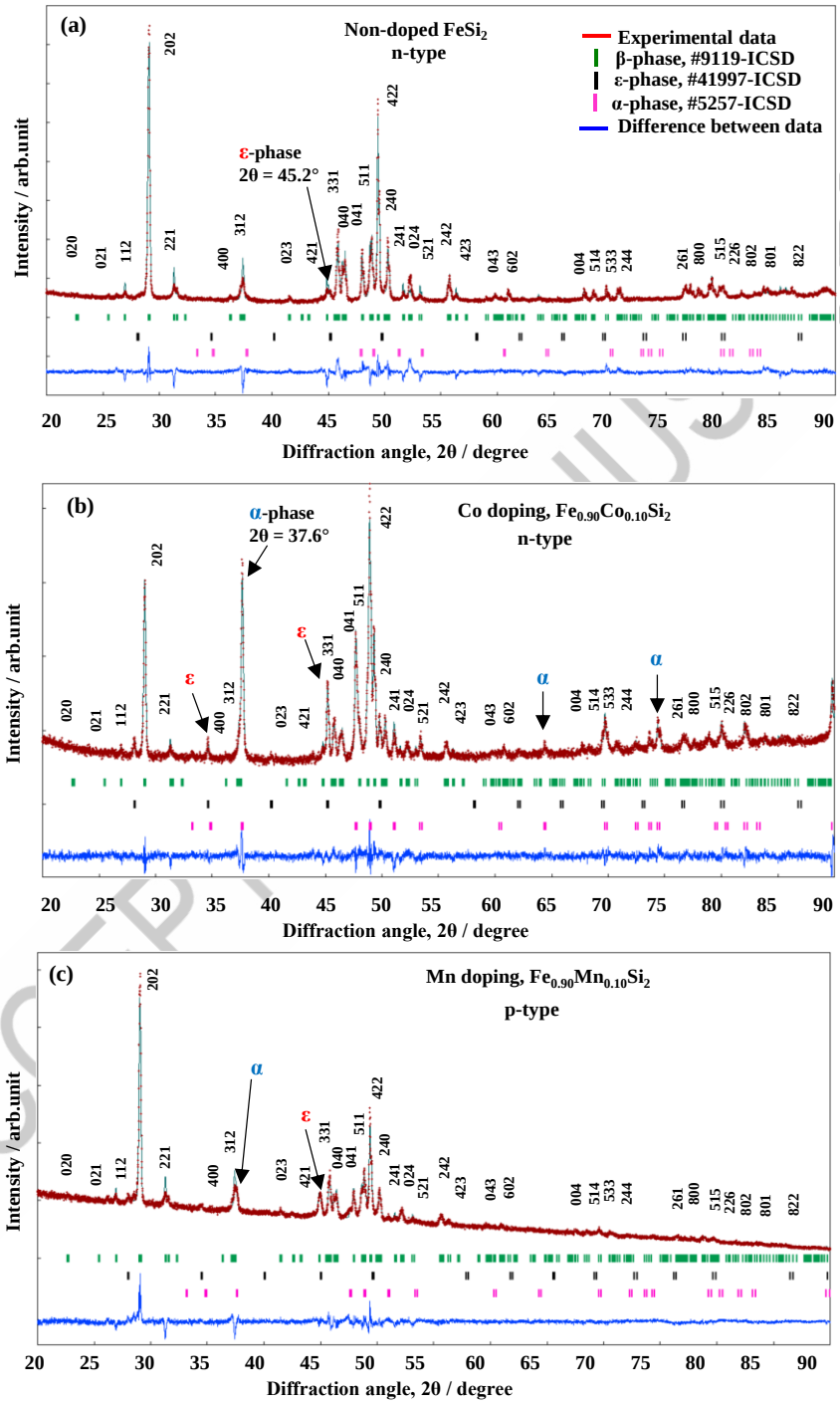

Fig. 3 Rietveld refinement of the X-ray diffraction data of **(a)** non-doped $FeSi_2$, **(b)** with 10%Co doping, and **(c)** with 10% Mn doping. The index peaks are the peaks of the semiconducting β-phase. The arrows indicate the peaks of impurity phases (ε and α-phases). Reproduced from the Ref. [43] © *Elsevier 2023*, and Ref. [44] © *Elsevier 2024.*

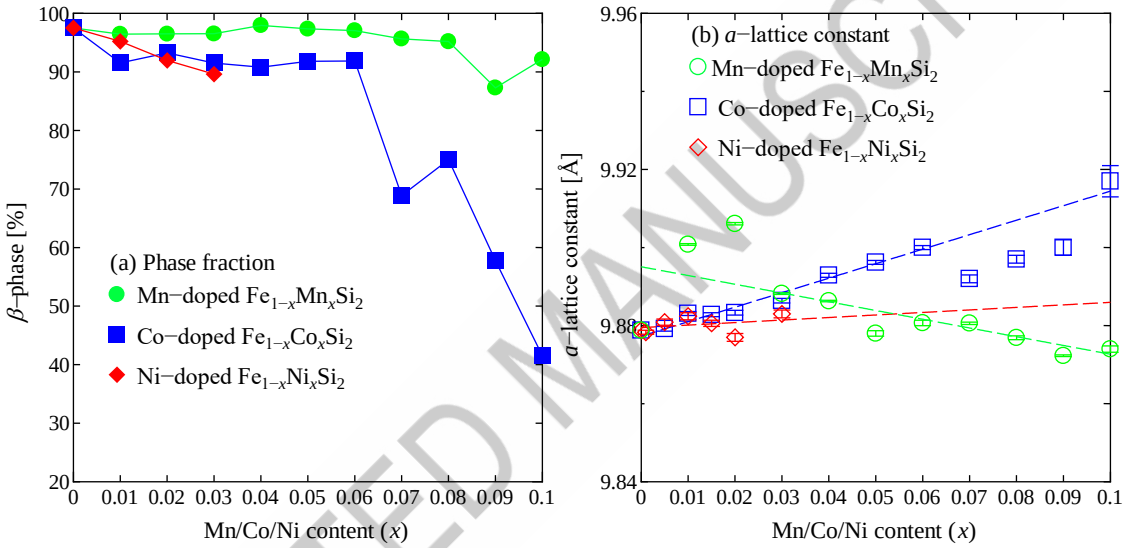

Fig. 4 (a) The variation of β-phase and **(b)** *a*-lattice constant dependence of the doping levels of Mn, Co, and Ni obtained by the Rietveld analysis. The data plotted in this figure are collected from Refs. [43,44,51].

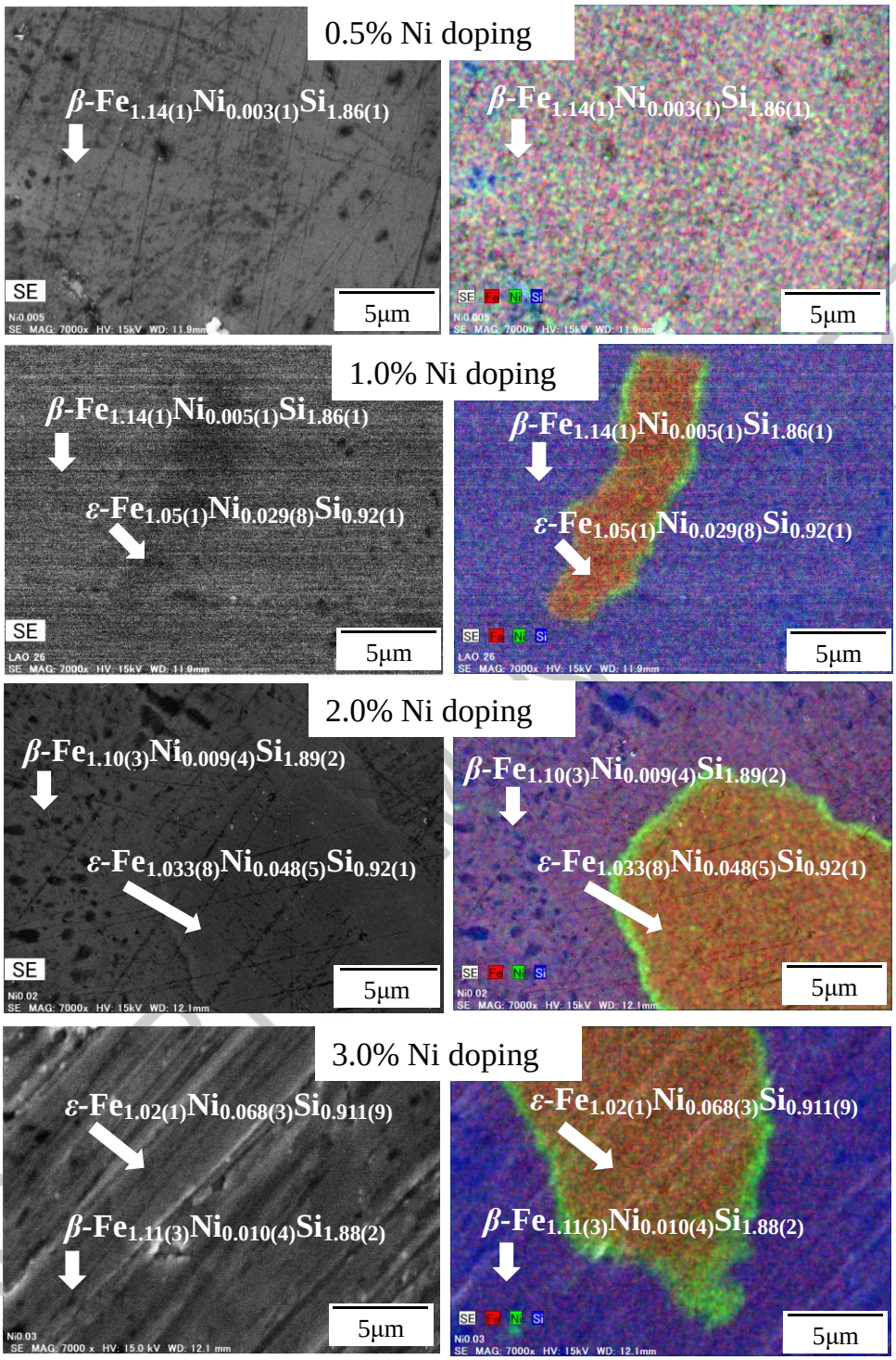

Fig. 5 SEM-EDS mapping to observe the variation in microstructure of Ni-doped β-$FeSi_2$. The Ni doping level is from 0.5% to 3%. The Fe elements are mapped in red, Ni in green, and Si in blue. Reproduced from Ref. [53] *© 2023 by the authors, licensed under CC BY 4.0* (https://creativecommons.org/licenses/by/4.0/)

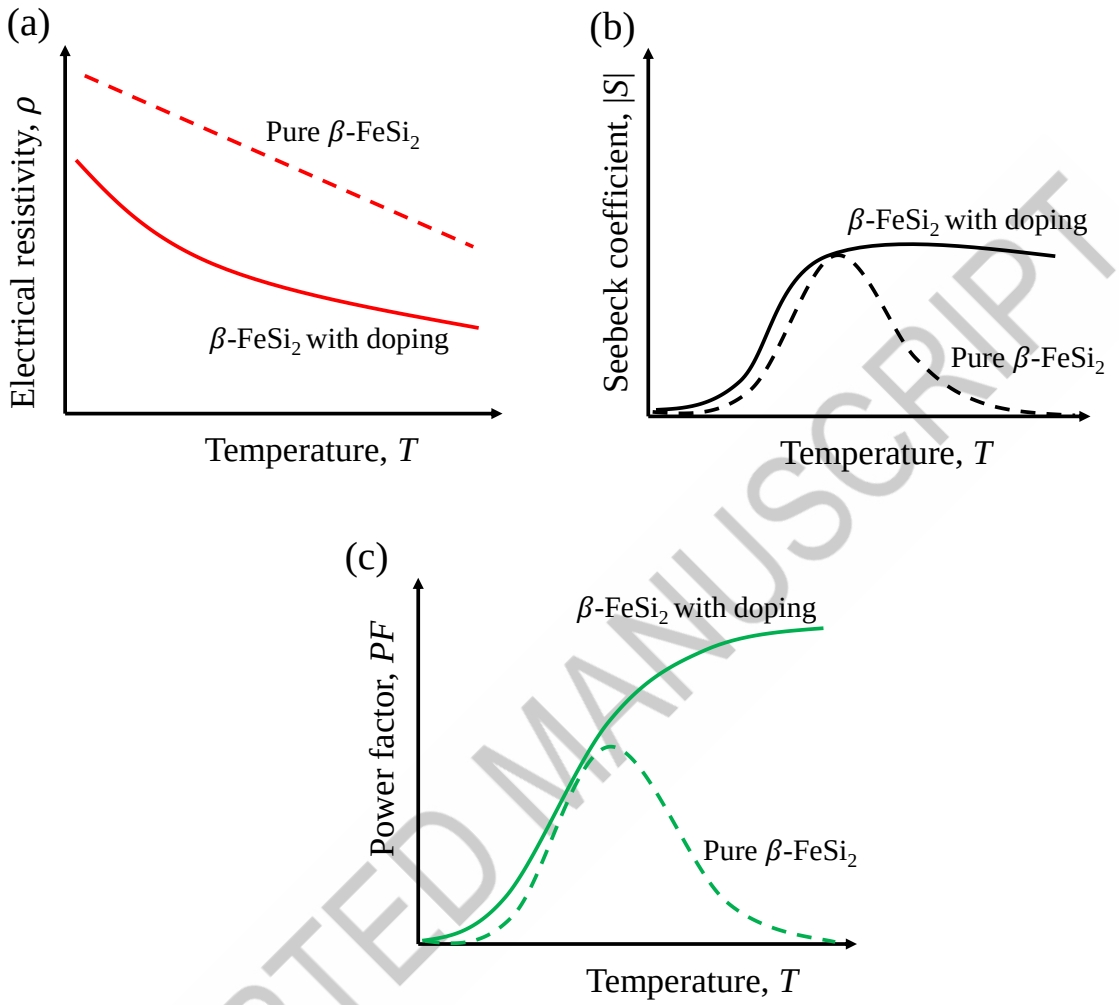

Fig. 6. Schematic illustration of the transport properties improvement of β-$FeSi_2$ with doping. **(a)** Decrease in electrical resistivity (ρ), **(b)** Improvement of Seebeck coefficient (S) at high temperature region, and **(c)** Enhancement in power factor ($PF = S^2\rho^{-1}$).

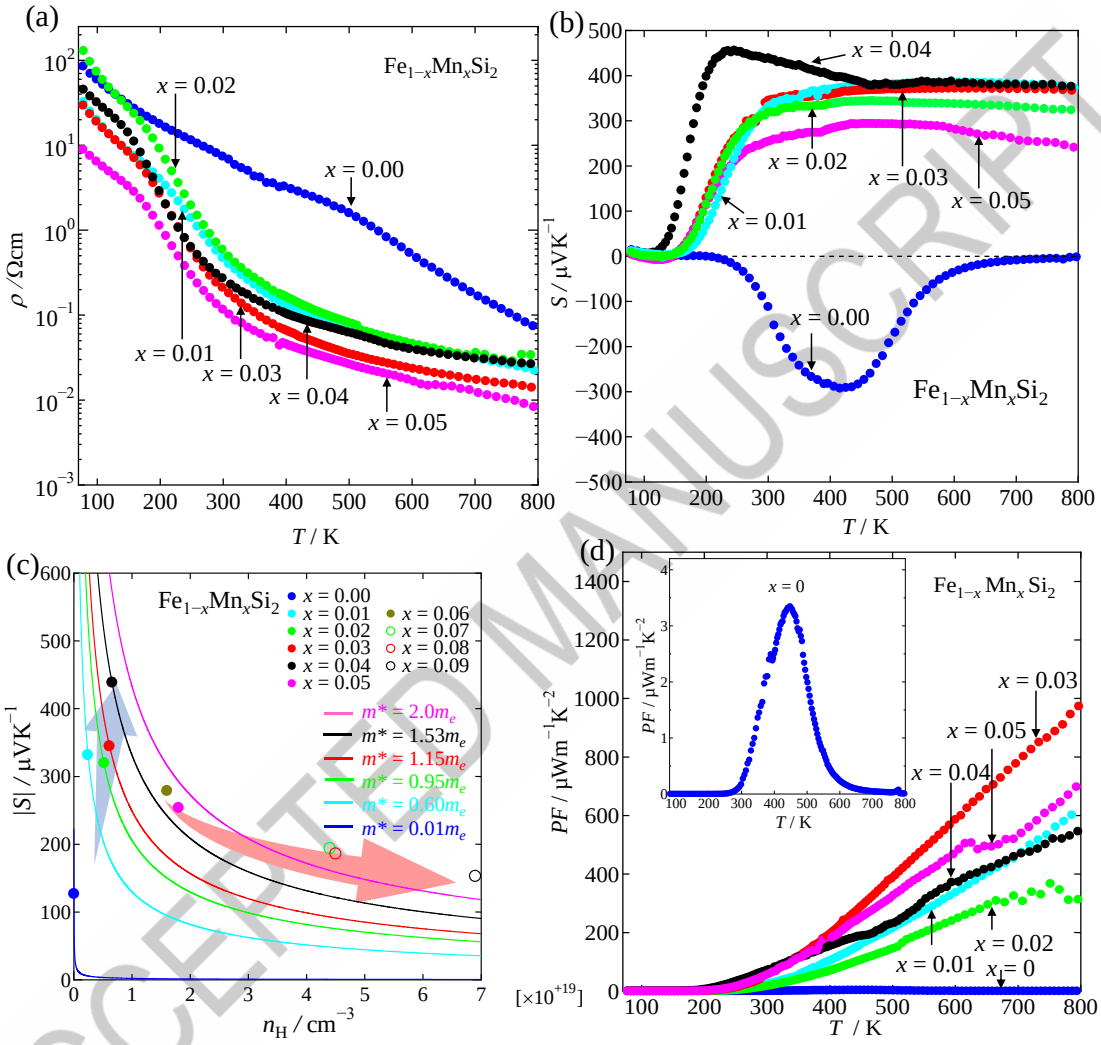

Fig. 7. Transport properties of β-$Fe_{1-x}Mn_xSi_2$ ($0 \leq x \leq 0.05$). **(a)** Temperature dependence of electrical resistivity ρ, and **(b)** Seebeck coefficient S. **(c)** Seebeck coefficient vs. carrier density at room temperature. The solid lines are the calculated data from the Mott formula in **Eq. (1)** at various effective masses $m^* = xm_e$, where x is a variable and m_e is the static mass of the electron, i.e., 9.10938×10^{-31} kg. The blue arrow indicates that the Seebeck coefficient increases with doping level due to the increase in effective mass, while the red arrow indicates the Seebeck coefficient decreases with increasing carrier density. **(d)** Temperature dependence of power factor PF. Reproduced from Ref. [51]. © *Elsevier 2024.*

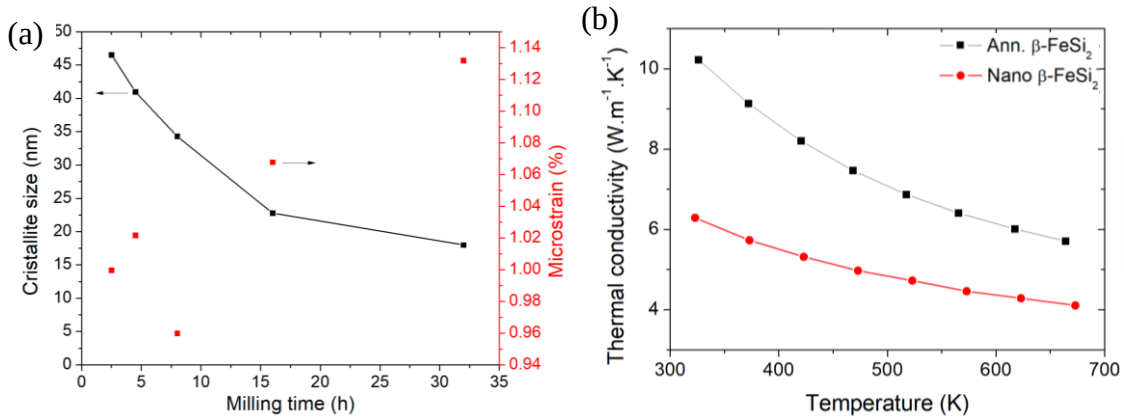

Fig. 8. The result of thermal conductivity reduction by nanostructuring with the milling process. **(a)** The crystallite size as a function of ball milling time (left axis) and micro-strain on the right axis. **(b)** The temperature dependence of the thermal conductivity of annealed β-$FeSi_2$ and nano β-$FeSi_2$ (fabricated by ball milling techniques). Reproduced from Ref. [67].

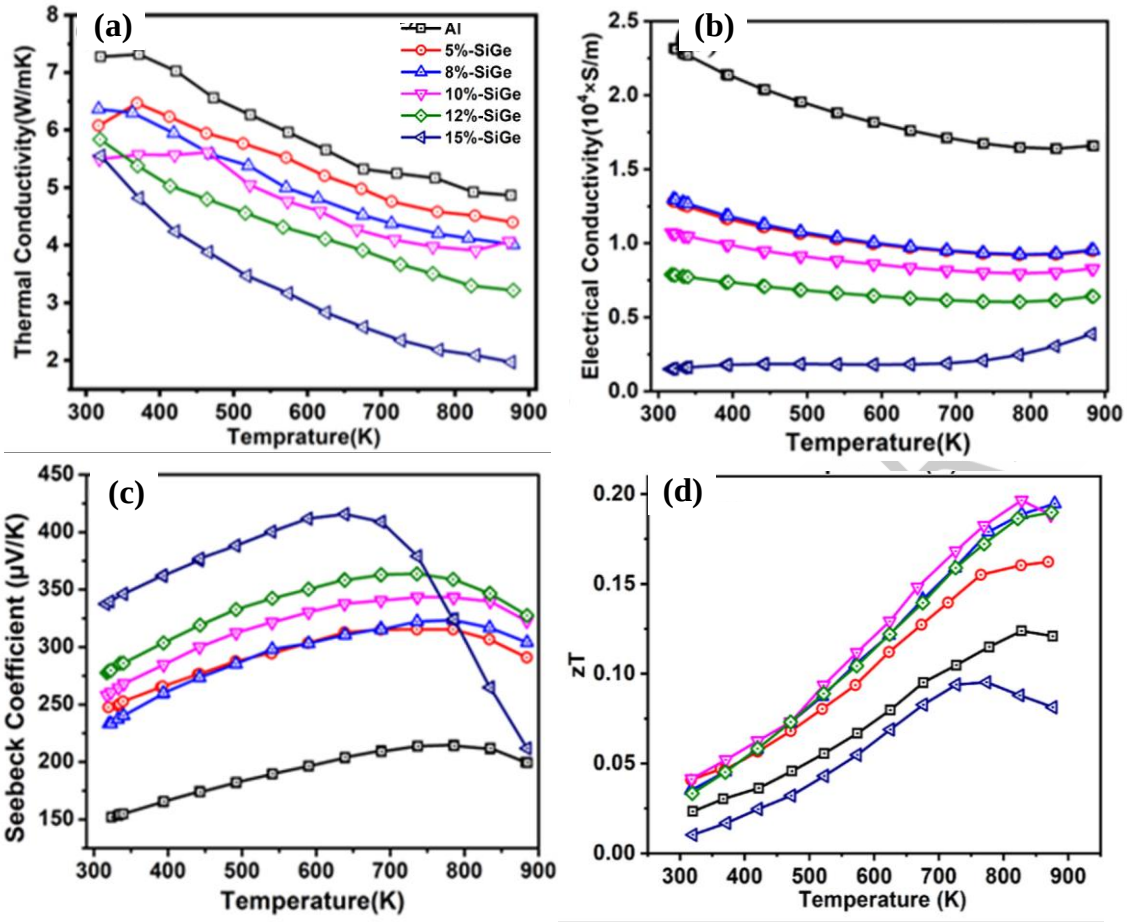

Fig. 9. Improved thermoelectric performance by reducing thermal conductivity of Al-doped β-$FeSi_2$ with the addition of Ge as a heavy element. **(a)** Total thermal conductivity, **(b)** electrical conductivity, **(c)** Seebeck coefficient, and **(d)** *ZT* values with temperature dependence. Reproduced from Ref. [45].

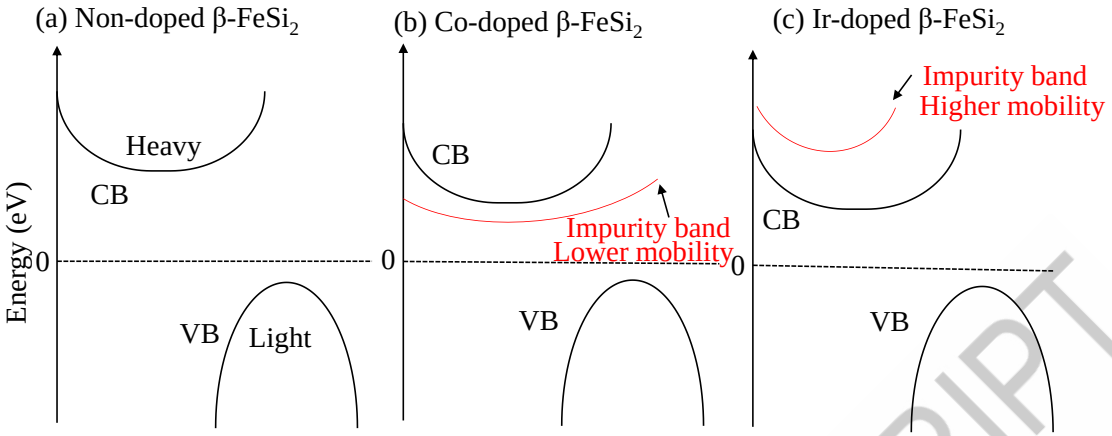

Fig. 10. Schematic of the band structure of **(a)** non-doped, **(b)** Co-doped, and **(c)** Ir-doped β-$FeSi_2$.

List of Tables

Table 1. Room temperature data of carrier density (n), mobility (μ), and calculated electrical resistivity (ρ) of n-type β-$FeSi_2$ with various dopants.

Dopant	Conduction type	n [cm^{-3}]	μ [$cm^2V^{-1}s^{-1}$]	ρ [Ωcm]	Reference
Non-doped	n	2.3×10^{16}	37	7.33×10^{0}	Sam *et al.* [33]
1% Co	n	1.8×10^{19}	5.9	5.88×10^{-2}	
3% Co	n	1.2×10^{20}	3.5	1.49×10^{-2}	
6% Co	n	4.2×10^{20}	1.9	7.82×10^{-3}	
1% Co	n	2.3×10^{20}	0.50	5.43×10^{-2}	Tani *et al.* [56]
3% Co	n	8.1×10^{20}	0.39	1.98×10^{-2}	
4% Co	n	1.9×10^{21}	0.4	8.21×10^{-3}	Cheng *et al.* [52]
8% Co	n	4.0×10^{21}	0.3	5.20×10^{-3}	
12% Co	n	1.1×10^{22}	0.3	1.89×10^{-3}	
16% Co	n	1.5×10^{22}	0.2	2.08×10^{-3}	
2.9% Co	n	7.6×10^{20}	0.26	3.16×10^{-2}	Birkholz *et al.* [66]
5% Co	n	1.9×10^{21}	0.35	9.39×10^{-3}	Nishida *et al.* [29]
3% Co	n	1.6×10^{18}	6.0	6.50×10^{-1}	Brehme *et al.* [80]
3%Co+1%Ni	n	1.4×10^{19}	25	1.78×10^{-2}	Sam *et al.* [57]
1% Ni	n	1.9×10^{19}	0.53	6.20×10^{-1}	Tani *et al.* [56]
3% Ni	n	4.7×10^{19}	0.27	4.92×10^{-1}	
1% Pt	n	4.8×10^{20}	0.65	2.04×10^{-2}	Tani *et al.* [62]
3% Pt	n	9.2×10^{20}	0.66	1.04×10^{-2}	
5% Pt	n	9.2×10^{20}	0.73	7.78×10^{-3}	
16% Ir	n	1.1×10^{22}	0.7	8.11×10^{-4}	Qiu *et al.* [38]

Table 2. Room temperature data of carrier density (n), mobility (μ), and calculated electrical resistivity (ρ) of p-type β-$FeSi_2$ with some dopants.

Dopant	Conduction type	n [cm^{-3}]	μ [$cm^2V^{-1}s^{-1}$]	ρ [Ωcm]	Reference
Non-doped	p	4.5×10^{17}	0.9	1.54×10^{1}	Tani *et al.* [56]
1% Mn	p	2.9×10^{18}	5.6	3.84×10^{-1}	Sam *et al*. [51]
3% Mn	p	6.1×10^{18}	4.3	2.38×10^{-1}	
5% Mn	p	1.8×10^{19}	3.3	1.05×10^{-1}	Sam *et al*. [44]
7% Mn	p	4.4×10^{19}	2.6	5.46×10^{-2}	
10% Mn	p	2.0×10^{19}	2.0	1.56×10^{-1}	
2% Al	p	2.0×10^{18}	2.0	1.56×10^{0}	Birkholz *et al.* [66]
1% Al	p	5.0×10^{19}	8.5	1.47×10^{-2}	Du *et al.* [58]
1.5% Al	p	1.2×10^{20}	9.0	5.78×10^{-3}	
2% Al	p	1.6×10^{20}	8.0	4.88×10^{-3}	

Table 3. Summary of ZT_{max} values of n-type β-$FeSi_2$ with various dopants using different processing methods. The order is classified from the low to high values of ZT_{max}.

Dopant	Processing methods	ZT_{max}	Temperature	References
Non-doped	Hot pressing (HP)	0.01	657 K	Kim *et al.* [79]
0.1% Ni	Arc melting	0.019	600 K	Sam *et al.* [53]
5% P	Ball milling/mechanical alloying (MA) + Pulse plasma sintering (PPS)	0.02	673 K	Dabrowski *et al.*[54]
2% P	MA+HP	0.033	672 K	Ito *et al.* [81]
2%Co+ 2%Y_2O_3	MA+HP	0.058	650 K	Ito *et al.* [77]
2% Co	MA+HP	0.06	600 K	Ur *et al.* [82]
2%Co+ 4%TiO	MA+HP	0.065	650 K	Ito *et al.* [78]
2%Co+ 4%SiO_2	MA+HP	0.078	650 K	Ito *et al.* [78]
1.77% Co	MA+HP	0.085	873 K	Redzuan *et al.* [83]
3% Co	Arc melting	0.099	720 K	Sam *et al.* [33]
5% Co + 4.2% Ge	HP	0.11	845 K	Kim *et al.* [79]
3% Pt	Spark plasma sintering (SPS)	0.14	847 K	Tani *et al.* [62]
3% Co	MA+PPS	0.15	773 K	Dabrowski *et al.*[54]
5% Co	MA+HP	0.182	923 K	He *et al.* [84]
5% Co	Gas-atomized sintering	0.22	900 K	Kimura *et al.* [85]
5% Co	SPS	0.25	940 K	Tani *et al.* [63]
6% Co	Rapid solidification +HP	0.25	908 K	Chen *et al.* [86]
8% Co	SPS	0.3	900 K	Cheng *et al.*[52]
3% Co + 1% Ni	Arc melting	0.31	720 K	Sam *et al.* [57]
6% Co + 5% Ru	SPS	0.33	900 K	Du *et al.* [47]
16% Ir	SPS	0.6	1000 K	Qui *et al.* [38]

Table 4. Summary of ZT_{max} values of p-type β-$FeSi_2$ with various dopants using different processing methods. The order is classified from the low to high values of ZT_{max}.

Dopant	Processing methods	ZT_{max}	Temperature	References
Non-doped	Ball milling/mechanical alloying (MA) + Pulse plasma sintering (PPS)	0.01	673 K	Dabrowski *et al.*[54]
5% Cr	Hot pressing (HP)	0.03	657 K	Kim *et al.* [79]
24% Zr	MA+HP	0.03	1070 K	Ito *et al.* [12]
7% Al	MA+PSS	0.06	773 K	Dabrowski *et al.*[54]
8% Mn	MA+PSS	0.06	773 K	Dabrowski *et al.*[54]
5% Mn	Arc melting	0.07	800 K	Sam *et al.* [44]
3% Al	MA+HP	0.08	873 K	He *et al.* [84]
5% Mn	Gas-atomized sintering	0.10	900 K	Kimura *et al.* [85]
3% Mn	Arc melting	0.12	800 K	Sam *et al.* [51]
2% Al	Spark plasma sintering (SPS)	0.18	850 K	Du *et al.* [58]
10% Mn	SPS	0.21	1040 K	Tani *et al.* [87]
2% Al + 20% Os	SPS	0.35	850 K	Du *et al.* [58]

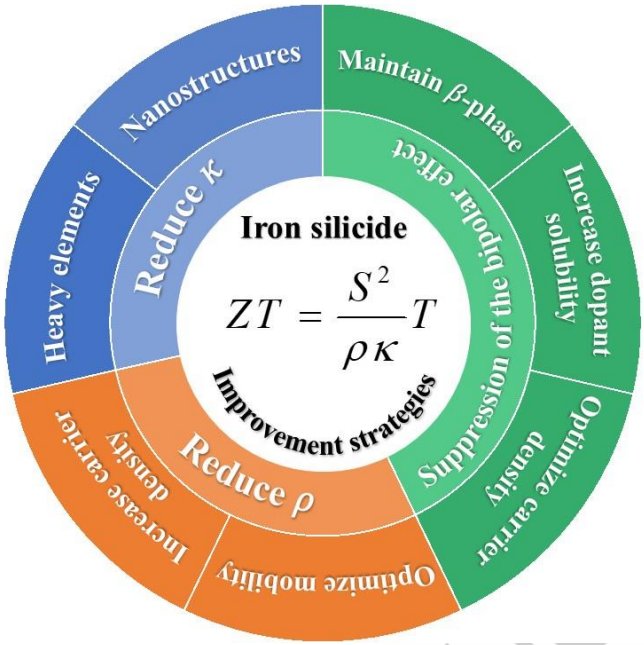

Graphical Abstract

Sopheap Sam, PhD, is a lecturer-researcher in the Department of Mechanical and Industrial Engineering and the Research and Innovation at the Institute of Technology of Cambodia. He obtained his Doctor of Engineering in Materials Science Frontier, Yokohama National University, Japan, in 2023. He was a Postdoctoral researcher at the National Institute for Materials Science, Japan, from 2023-2025. His research interests include thermoelectric materials and micro/nanostructures for controlling transport properties.

Sreypich Say, PhD in Biomedical and Engineering, Tokyo Medical and Dental University, Japan, in 2024. She was a Postdoctoral researcher at Keio University, Japan, from 2024-2025. In June 2025, she joined the University of Puthisastra as a Full-time lecturer for the Master's Program. Her research interests include functional materials and nanostructured materials.

Kosuke Yamazaki, PhD. candidate in Materials Science and Engineering, Graduate School of Engineering Science, Yokohama National University, Japan, from 2023. He graduated from the Department of Materials Science and Engineering at the National Defense Academy of Japan in 2019. In 2021, he enrolled as a master's student in the Graduate School of Science and Engineering at Yokohama National University, Japan. His research interests include thermoelectric properties for half-Heusler alloys.

Hiroshi Nakatsugawa, PhD, is an Associate Professor at the Graduate School of Engineering, Yokohama National University, Japan. He earned his Doctor of Engineering degree in the field of Production Engineering from Yokohama National University, Japan in 1998. From 1998 to 2001, he served as a Research Assistant at Yokohama National University, Japan. He has held his current position since 2001. His research focuses on the thermoelectric properties, crystal structures, and magnetic properties of transition metal oxide materials.

Impact Statement

This review covers the observation of structural transition and strategies to enhance electrical and thermoelectric properties of metal-doped iron silicides, providing insights for future research to improve material performance.